CHARGE STRUCTURE OF A QUASIPARTICLE IN GRAPHITE MEASURED WITH INELASTIC X-RAY SCATTERING

BY

JAMES PHILLIP REED

DISSERTATION

Submitted in partial fulfillment of the requirements
for the degree of Doctor of Philosophy in Physics
in the Graduate College of the
University of Illinois at Urbana-Champaign, 2009

Urbana, Illinois

Doctoral Committee:

Professor Tai-Chang Chiang, Chair
Associate Professor Peter Abbamonte, Director of Research
Professor Michael Stone
Professor James Wiss

Abstract

The following work consists of three related topics. First, we demonstrate a multi-dimensional, attosecond-resolution, real-space electron density imaging technique. We apply the technique to the energy-loss spectra of graphite, which we measured using inelastic X-ray scattering at the Advanced Photon Source in Argonne, IL. The results are images of the anisotropic charge density cloud that surrounds a test charge to form quasiparticles in graphite. We are able to watch the anisotropic charge structure of a quasiparticle as it is born and evolves in real-space and at 10 attosecond intervals. We then set the dynamical part in motion to test how rigidly the quasiparticle maintains its structure with increasing velocity. Second, we perform numerical integration on the charge density data to obtain the size of the static background dielectric constant, ϵ_∞. We offer a possible explanation for some of the discrepancies between current experiments and theoretical work on graphene based on our findings from graphite. Lastly, we introduce a conversion technique as a work in-progress which enables us to examine the 2-dimensional density-density Green's function from 3-dimensional data.

For mother and father.

Acknowledgments

So many people have helped me along the way in the course of the last six years that it is hard to acknowledge everyone, but here goes.

Special thanks to Peter Abbamonte, my advisor, who has a rare gift of both enormous wisdom and enormous patience. He saved me from the disillusionment caused by my previous physics advisor and showed me what it really means to be a physicist. I would not be here without him and his kind and friendly encouragement.

I would like to thank Diego Casa and Thomas Gog at the APS for keeping our beam times running so smoothly and for being so forgiving when I would break stuff in station C. Their insight and troubleshooting abilities are second to none. And thanks to Young Il Joe and Yu Gan for helping run everything during our beam time and for helping collect a good portion of my data.

Thanks to Bruno Uchoa for all of our discussions and for his vast knowledge of what seems to be every paper ever written on graphene. His understanding of the topic of graphene helped steered us out of our theory quagmire.

To Joe Gezo, Kevin Mantey, Meng Liang, Alice Bridgeman, Kevin Inderhees, Dan Vanderveld, and Josh Sayre, thanks for all the 'lols,' for all of our wonderful, eye-opening discussion, and for helping me enjoy all of my free time. Without friends like these I don't think any of us would have made it through graduate school and all the trial and tribulations that go with it.

To my love, Ashley, I can't thank you enough for pushing me to write this damn thing even when I hated it, for supporting me, for cheering me on and for loving me even when I was crabby.

Thanks to Shari and David. I feel like the luckiest guy in the world because I had four loving parents, where some people are luck to have even one.

To my brother, Mike, thanks for always having crazy ideas and for all the love and protection he showed me when we were growing up.

And I thank my parents, who always supported and believed in me even when I didn't believe in myself, thanks.

Table of Contents

I Introduction

Motivation

The notion of a quasiparticle has been a key under-pinning of condensed matter physics for more than half a century. The quasiparticle concept still holds wide significance and is worthy of study using modern experimental and analytical techniques. The original conception of a quasiparticle by Landau in 1956 [1, 2] concerned how low energy excitations in a Fermi gas, near the Fermi energy, may be related to those of the non-interacting Fermi gas. Central to this problem is the concept of a Fermion quasiparticle, in which the individual particles near the Fermi energy are dressed by collective excitations of the other electrons in the system, forming a composite object that exhibits Fermi statistics and can be thought of as a new type of particle, albeit with a different mass and lifetime.

In an alternative perspective on this problem, Bohm, Pines and Nozières [3, 4, 5, 6, 7] showed that the interacting electron gas can be described as a system of weakly interacting electrons, provided they introduced new dynamical variables called plasmons. Plasmons are collective excitations of the electron density, similar to sound waves, and like Landau's conception are also valid quasiparticles. Other examples of quasiparticles in condensed matter are polarons, holons, spinons, phonons, holes, etc [8, 9, 10, 11].

In this body of research we use inelastic x-ray scattering to examine the internal charge structure of the so-called Fermion quasiparticles in a model semi-metal, namely single crystal graphite. Specifically, we reconstruct the local charge density cloud that surrounds and dresses electrons to form the Fermion quasiparticles. Graphite is a simple system whose single-layer component, graphene, is currently the subject of intense scientific research. We perform inelastic X-ray scattering to measure the

high energy ($E \gg t_\perp$) spectra of graphite (which coincidentally greatly resembles the spectra of graphene). The results of our analysis of the graphite data - both qualitative and quantitative - explore for the first time the underlying structure of a quasiparticle charge cloud and the dynamics of a quasiparticle's creation. We also test the rigidity and validity of a quasiparticle in motion to determine at what speed its structure breaks down and perform numerical calculations on the results of our analysis which offer possible explanations to current problems related to graphene.

The Quasiparticle

The Landau conception of the quasiparticle came about as a he was formulating a phenomenological theory to explain the macroscopic properties of low temperature liquid ^{3}He [2]. Fermi liquid theory ties together the ground state of a non-interacting electron gas to the low energy excitations of fermionic helium in the liquid ^{3}He system [12, 13]. The electrons in the non-interacting electron gas occupy progressively higher-energy plane wave states constrained by the Pauli exclusion principle and characterized by a wave vector $\vec{k}$. These form a "Fermi sea" of occupied states with a distinct cutoff at the Fermi wave vector k_F. The scientific leap which Landau made is that the energy states of this simple non-interacting gas share a one-to-one correspondence with the complicated states of the interacting electron system in liquid ^{3}He. In other words, if we start with a non-interacting fermion gas of electrons, we can gradually transform its ground state into the ground states of liquid ^{3}He by adiabatically turning on the interaction. Moreover, the slow tuning-on of the interaction connects the excited states of the two system in the following way: an additional particle added to ground state of the non-interacting electron gas with wave vector $\vec{k}$ ($|\vec{k}| > k_F$) puts the non-interacting electron gas into a new eigenstate. If we now adiabatically tune-in the interaction as described before, this new eigenstate of the

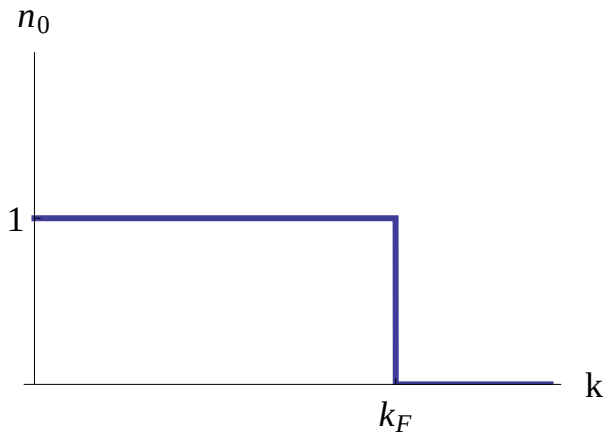

Figure 1.1: A diagram of the Fermi Dirac distribution, which describes the occupation of states of a non interacting gas at zero temperature. The abrupt cutoff at the k_F is called the "Fermi surface" above which no particles reside.

non-interacting electron gas must correspond to an eigenstate of the interacting electrons of liquid ^{3}He and the difference between the liquid helium ground state and its new eigenstate must have wave vector $\vec{k}$ to conserve momentum [2].

This added excitation with definite momentum is what Landau called a quasiparticle. It is no longer a simple plane wave as in the case of the non-interacting electrons, but is a spatially extended object formed by the addition of a particle at $\vec{k}$ and the perturbed disturbance of other particles that cling to it. It has similar characteristics to its single particle brother: it is a fermion, it has a charge, and it has a mass. However, these low energy quasiparticle excitations are generally short-lived except in the vicinity of the Fermi surface where their lifetime becomes quite long. The Landau quasiparticle concept holds up well so long as the k_BT is well below E_F, the adiabatic addition of the interaction does not cause a phase transition, and excitations are low-lying and fairly close to the ground state. The theory was hugely successful in qualitatively describing the thermodynamic properties of not only ^{3}He,

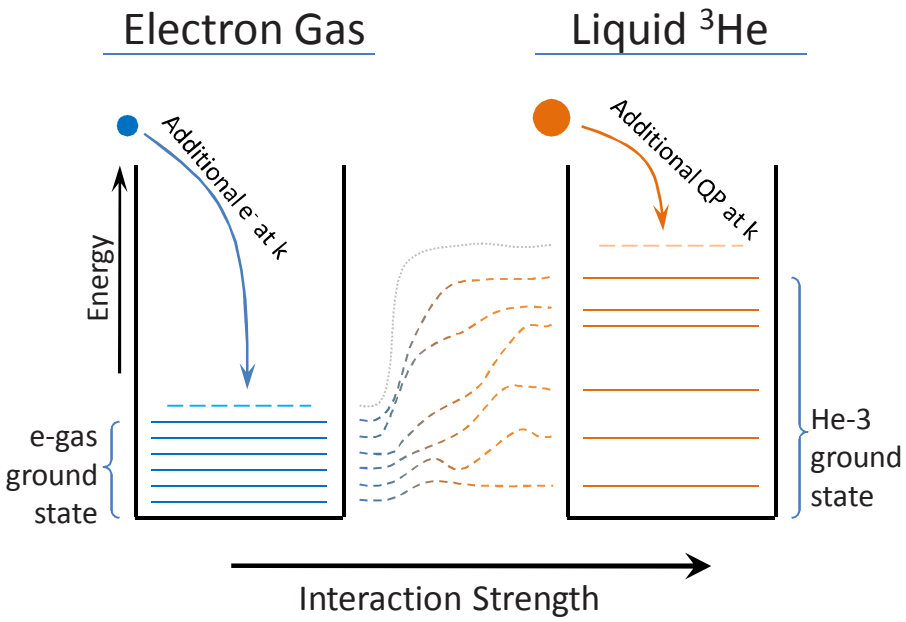

Figure 1.2: The eigenstates of the non-interacting electron gas are connected one-to-one with the eigenstates of the Fermions in liquid ^{3}He as the interaction between electrons is adiabatically turned on. In a similar manner, the addition of an electron in a plane wave eigenstate with momentum $\vec{k}$ to the electron gas necessitates a correspondence of an additional quasiparticle in a very complicated eigenstate with momentum $\vec{k}$ to the liquid helium system.

but also nuclear matter as well as the electrons in most metals.

Pines and Nozières, two contemporaries of Landau, were also studying what kinds of elementary excitations an interacting electron system could support in a given phase. However, their efforts concentrated not on the very low energy, ultra cold, single-particle excitation as in Landau's work, but rather on the high-energy collective excitations and how they can screen and interact with other electrons in the system. Their basic premise is that a large number of electrons confined to a small enough

volume will not interact via Coulomb's law,

$$V(r) = \frac{e^2}{r}$$

but rather by a weaker repulsive interaction given by the Yukawa potential,

$$V_{eff}(r) = \frac{e^2}{r}\,\mathrm{e}^{-k_0 r}. \tag{1.1}$$

This interaction is greatly reduced in magnitude and has a much shorter range than the bare Coulomb potential as seen in Figure 1.3, resulting in the electrons behaving as if they are nearly non-interacting. This interesting result comes about because

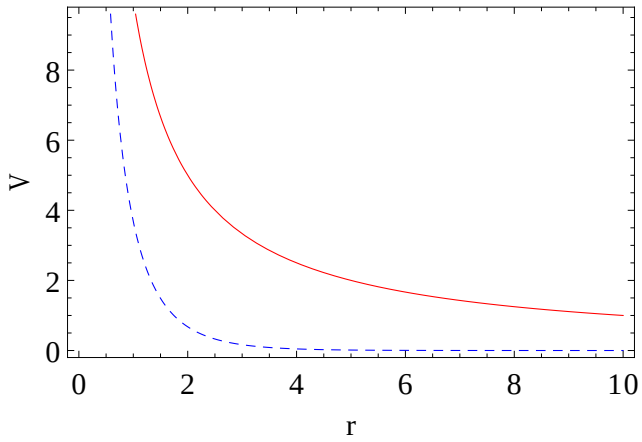

Figure 1.3: The bare Coulomb and screened Coulomb interactions are shown as solid and dashed lines respectively. The axes are in arbitrary units with $k_0 = 1$ used for the Yukawa potential from equation (1.1).

the closely packed electrons in a solid (as opposed to a neutral gas) try to avoid one another as much as possible because of their Coulomb repulsion. To this end, each electron surrounds or "dresses" itself with a cloud of positive charge (i.e. reduced electron density), $\rho_{cloud}(\vec{r})$, that acts to screen out the electric field and charge of the electron.

The density cloud $\rho_{cloud}(\vec{r})$ is not just a simple mathematical modification to the electron's interaction. When an electron is excited out of the Fermi sea the cloud surrounds the electron; together they form a new, rigid construct with a finite spatial extent (as opposed to an electron point particle) that carries the same momentum, spin, and fermionic properties of the electron at its core. Just like in the Landau case, the system has formed a quasiparticle.

In the original work by Pines and Nozières the quasiparticle is a spherically symmetric structure [3, 4], which one might expect for a group of confined electrons without a structured lattice. In reality though, how the electrons are influenced by the underlying atomic lattice will have a great effect on the quasiparticle, giving it structure and affecting its size, shape, and symmetry. Moreover, the quasiparticle structure retains its rigidity as it travels through the medium, pushing aside charges in its path. Moving in this manner, the quasiparticle cloud, $\rho_{cloud}(\vec{r}, t)$, creates a current, $J_{cloud}(\vec{r}, t)$, described by the continuity equation,

$$\nabla \cdot J_{cloud}(\vec{r}, t) + \frac{\partial \rho_{cloud}(\vec{r}, t)}{\partial t} = 0. \tag{1.2}$$

The current, $J_{cloud}(\vec{r}, t)$, mimics a "backflow" of charge caused by the distortion of the medium around the electron. This is much like dragging a marble ball through a viscous fluid; the fluid moves around and fills in the space behind the marble, but the marble is harder to accelerate due to the momentum of fluid. The same occurs for the backflow around the electron; it has a momentum associated with it which thereby changes the inertial properties of the quasiparticle, changing its mass from the bare electron mass, m, to its effective mass m^*.

The question then becomes, what quantity describes these quasiparticle density clouds? Pines and Nozières showed that $\rho_{cloud}(\vec{q})$ is directly related to the electron

density-density correlation function [14], $\chi(\vec{q},\omega)$ via

$$\rho_{cloud}(\vec{q},\omega) = -e\,V(q)\,\chi(\vec{q},\omega), \tag{1.3}$$

such that $\rho_{cloud}(\vec{r},t)$ is just the Fourier transform of $\rho_{cloud}(\vec{q},\omega)$ in space and time. It follows that studying the properties of $\chi(\vec{q},\omega)$ by measuring the spectral function of the collective excitations, such as plasmons, of the system of interest, we garner knowledge of the quasiparticle's electron density cloud.

The quasiparticle concept is vital to the success of solid state physics because of the corollaries resulting from the above properties. The weakened Coulomb interaction, V_{eff}, of the quasiparticles permit us to make the independent electron approximation that produces rigid energy bands which are robust to a change in the number of particles in the system. A finite quasiparticle weight in the spectral function is required to produce the discontinuous occupation at the Fermi surface. If we combine the fact that electron quasiparticles still exhibit Fermi statistics with their rigid band structure, we can deduce the power law temperature dependence of specific macroscopic thermodynamic quantities, such as a T^2 dependence of resistivity, a linear T dependence of the specific heat, etc. Moreover, deviations from these temperature dependence laws points to a breakdown of the quasiparticle concept and typically occurs in systems that exhibit exotic physics such as the high-T_c cooperate superconductors [15] and some heavy Fermion materials [16].

So how can we put such a varied and important concept to the measure? We choose a system that has an simple and yet elegant structure that is relevant to current physics and which still forms the quasiparticle structures we are interested in investigating: graphite.

Atomic Structure

Carbon is all around us. It forms the long chains, such as hydrocarbons, that make organic life possible and composes much of the materials, such as plastics and wood, we use in our daily lives. In its elemental form it can take the form of an amorphous powder or an impressive solid - it ranges from ultra-hard, beautiful diamonds to tiny fullerene nanotubes that have a tensile strength (22.2 GPa [17] to 150 GPa [18]) many times greater than steel (0.45 GPa to 1.2 GPa [19]) or Kevlar (3.6 GPa to 3.8 GPa [20]). Somewhere in between these two extremes it forms a unassuming, dull gray, laminar crystal called graphite, which has captivated the attention of solid state physics.

To examine the stacked, honeycomb lattice of graphite we begin by looking at the

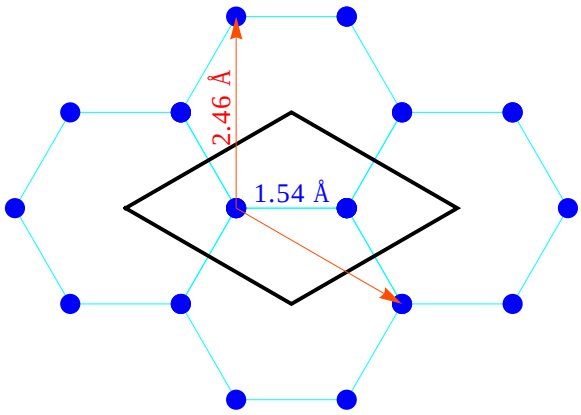

Figure 1.4: The real space lattice of a graphene sheet. The dots represent Carbon atoms and the lines are the bonds between atoms. The arrows indicate the in-plane Bravais lattice vectors and the black diamond outlines the two atom unit cell. The key points of the Brillouin zone are indicated as Γ, K, K′, and M.

lattice structure of a single layer of graphite, called a graphene sheet, and then building our way back up to the full 3-dimensional graphite. Graphene has a simple base unit cell of two carbon atoms, spaced 1.54 Å apart along the x-axis, with in-plane Bra-

vais lattice vectors of $\vec{a}_1 = (0.0\,\text{Å},\ 2.46\,\text{Å},\ 0.0\,\text{Å})$ and $\vec{a}_2 = (2.13\,\text{Å},\ \text{-}1.23\,\text{Å},\ 0.0.\,\text{Å})$, angled 120° apart. This simple unit cell with corresponding Bravais lattice vectors creates the famous hexagonal honeycomb structure displayed in Figure 1.4.

The addition of the third dimension requires us to specify which stacking of graphite is being discussed. Although there exists $2^{N/2}$ combinations of different stack-

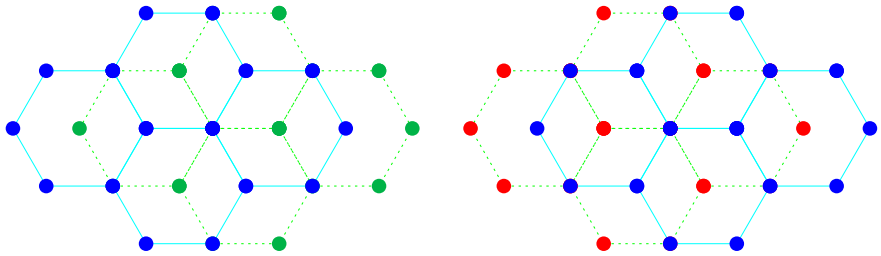

Figure 1.5: Diagrams of the $ABAB$ and $ACAC$ stacking types. The blue dots connected with solid lines are the carbon atoms of the A plane, the green (left side) and red dots (right side) connected with dotted lines are the carbon atoms of the B and C stacking respectively.

ings for the N layers; typically the discussion is restricted to the $ABAB$ (or $ACAC$, a 180° spin of $ABAB$) stacking type, where the stacking is subsequently repeated for all layers. The unit cell for the $ABAB$ stacking of graphite is a perpendicular parallel prism with the top and bottom face being the same as the 2-dimensional unit cell shown in black in Figure 1.4. The third Bravais lattice vector lies solely along the z-axis as $\vec{a}_3 = (0.0\,\text{Å},\ 0.0\,\text{Å},\ 6.701\,\text{Å})$. Using these Bravais vectors we can construct the entire lattice of the graphite crystal by adding a copy of the 3-dimensional unit cell (as seen in Figure 1.6) at each of the vectors $\vec{R} = n_1\vec{a_1} + n_2\vec{a_2} + n_3\vec{a_3}$, where n_1, n_2, and n_3 are integers.

The reciprocal space representation of graphite is very similar to its real space

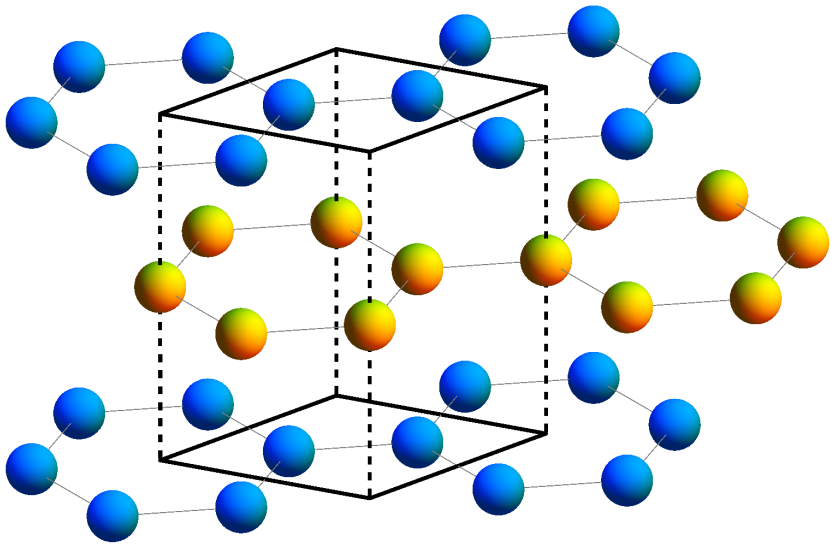

Figure 1.6: The 3-dimensional stacking of graphite with the unit cell drawn in black. The top and bottom blue layers are the A stacking and the middle yellow layer is the B stacking.

structure. The reciprocal lattice vectors obtained from the canonical equation [21]

$$\vec{b}_i = 2\pi \frac{\vec{a}_j \times \vec{a}_k}{\vec{a}_i \cdot (\vec{a}_j \times \vec{a}_k)}$$

where Levi-Civita cyclical permutations are assumed, are $\vec{b}_1 = (1.47\,\text{Å}^{-1}, 2.55\,\text{Å}^{-1}, 0.0\,\text{Å}^{-1})$, $\vec{b}_2 = (2.95\,\text{Å}^{-1}, 0.0\,\text{Å}^{-1}, 0.0\,\text{Å}^{-1})$, and $\vec{b}_1 = (0.0\,\text{Å}^{-1}, 0.0\,\text{Å}^{-1}, 0.94\,\text{Å}^{-1})$. The only significant difference in qualitative features (symmetries, angle, etc.) between the direct and reciprocal lattice is that the in-plane reciprocal lattice vectors, $\vec{b}_1$ and $\vec{b}_2$, are 60° apart instead of 120°.

The in-plane bonds holding the carbon atoms together come from hybridization of one s orbital with two p orbitals. These sp^2 hybridized orbitals form the three trigonal in-plane bonds separated by 120°. The remaining p orbital sticks perpendicularly out of plane and bonds covalently to nearby carbon atoms to create the π band, which is half filled. The stacked graphene layers within graphite are weakly held together by a van der Waals-like interaction [22] , this allows them to be cleaved apart of slip

past one another such as pencil lead sliding off onto a piece of paper.

Band Theory

Graphite

The description of graphite and graphene up to this point has been mostly on the atomic structure and reciprocal lattice, which are fairly straightforward. However, the focus of our research involves the properties of the electrons and understanding how they interact with each other in the context of the underlying atomic lattice. Therefore, we must understand the band structure of graphite. The band structure of the π and π^* conduction bands of graphite was first described using a tight-binding approach by the equations:

$$E - E_0 = H_0 - \frac{1}{2}\gamma_1\Gamma \pm \sqrt{\frac{1}{4}\gamma_1^2\Gamma^2 + \gamma_0^2|S|^2} \tag{1.4}$$

$$H_0 = -2\gamma_0\bigg(\cos(2\pi q_y a) + 2\cos(\pi\sqrt{3}q_x a)\cos(\pi q_y a)\bigg) \tag{1.5}$$

$$S = \mathrm{e}^{-2\pi \mathrm{i} q_x a/\sqrt{3}} + 2\cos(\pi q_y a)\,\mathrm{e}^{\pi \mathrm{i} q_x a/\sqrt{3}} \tag{1.6}$$

$$\Gamma = 2\cos(\pi q_z c) \tag{1.7}$$

by Wallace [23] in 1947, where γ_0 and γ_1 are the nearest neighbor overlap integral energies for in-plane hopping and inter-plane hopping respectively. Although the band structure was first theorized in the l947, graphite has been used experimentally for quite some time prior, notably by Compton in 1923 in his archetypal work on the scattering process that bears his name [24]. The original inception of graphite's band structure was for the most part correct, though later theories by Slonczewski and Weiss [25], and McClure [26] refined and improved upon it by including more overlap integrals and transitions between second- and also third-nearest neighbor carbon atoms.

The choice of sign in equation (1.4) corresponds to the upper π or lower π^* band of graphite. These two bands narrow to cones near the K and K' points of the Brillouin zone where they touch at zero energy, forming 'pockets' of Fermi surface. Along the

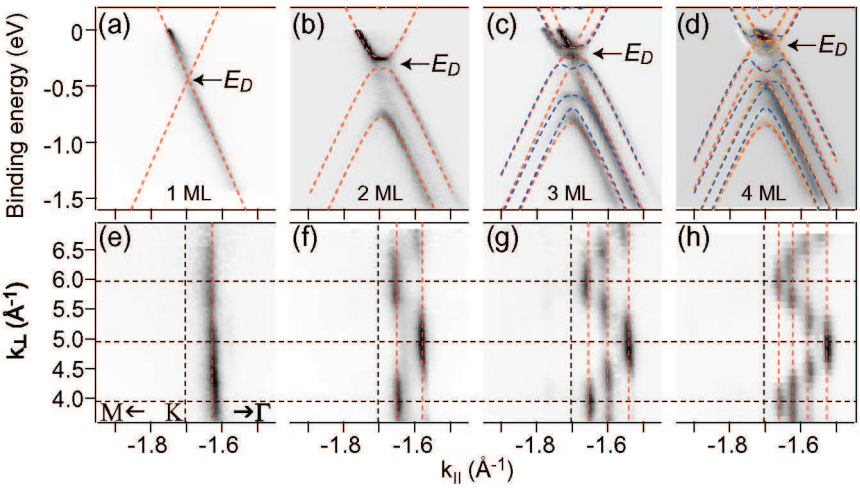

Figure 1.7: Images (a) through (d) show the inflation of singular Dirac point to the pockets of Fermi surface as the number of layers increases from 1 to 4. Images (e) through (h) show the formation of the band in the k_z direction as a function of the number of layers of graphene. By the fourth layer the band has become clearly defined in this ARPES study by Ohta, et al [27].

q_z direction the band forms a ubiquitous $2t_\perp \cos(q_z c)$ structure for any given q_x and q_y. This band materializes rapidly as individual layers of graphene are stacked up as shown in ARPES experiments [27].

Graphene

Recently it is not graphite that has been the subject of exhaustive research, but rather graphene. Production of a single layered graphene sheet was first achieved by a micromechanical exfoliation technique created by Novoselov [28] in 2005. Aside

from being an easily accessible two dimensional system for experimentalists, graphene also displays very unique properties in its band structure. The most notable of these is the linear energy dispersion, much like the Dirac equation from relativistic quantum mechanics, at the K and K' points of the Brillouin zone. Moreover, where the graphite band crossings at the zone corners form pockets, graphene's bands cross to form a singular point in the Fermi surface. These have been nicknamed the "Dirac points" due to the energy dispersion and the electrons that occupy the local vicinity in momentum space around the Dirac points are called "Dirac fermions."

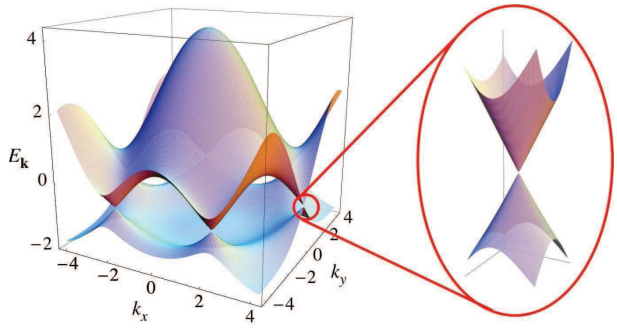

Figure 1.8: The π and π^* band structure of graphene within the first Brillouin zone. An image of the linear dispersive band crossing has been enlarged on the right [29].

Recent Work

Graphene provides a unique opportunity to study a variety of phenomena which take advantage of its unique band structure such as the quantum hall effect, relativistic Dirac fermions, and new novel gated devices like field effect transistors. The quantum hall effect in a multi-layer graphene film was discovered and studied by Novoselov in 2004 [30]. The results of their study showed not only that graphene is a truly 2-dimensional system but also that the charge carries in graphene are massless Dirac

fermions which maintain finite conductivity even as the Fermi energy approaches zero as predicted by Fradkin in 1986 [31]. Additionally, because the electron energy bands in graphene disperse linearly, the electron velocity in graphene is a constant ($v \approx 10^6 m/s$) akin to the speed of light for photons. And, as a result of the Hamiltonian mirroring the vanishing mass limit of the Dirac equation we can pull results straight from relativistic quantum mechanics such as the electrons tunneling through potential barriers of any size with no reflected components, called the Klein paradox [22]. This effect, observed in graphene [22], helps boost the conductivity of the carriers, both the electrons and holes.

The use of graphene in device technology is still in its infancy, but shows great promise. By pattering and gating a single layer of graphene, it is possible to make a field effect device many times thinner than those currently in production [32]. Current research shows the promise of being able to enhance and possibly even replace silicon devices and the Moore's law scaling dogma that goes with silicon. Research is already underway to characterize the electronic and noise properties [33] of gated (top and bottom) graphene transistors as well as producing tunnel field-effect transistors from graphene nanoribbons that have 5 times greater speed and 20 times less power dissipation [34] than conventional MOSFETs. Additionally, recent endeavors have shown success in opening a band gap in graphene, tuning it from a semimetal to a semiconductor, by either creating controlled ripples in the surface of graphene which mimic a period potential that induces an effective gauge field [35], or by engineering strain into the graphene structure which essentially functions as a strong uniform magnetic field [36]. Even beyond electronic engineering, graphene has been shown to be useful in optics where researchers have exploited its unique optical properties to create a photon detector, which despite being only one atomic layer thick, absorbs about 2% of incident photons over a broad range of wavelengths at a response

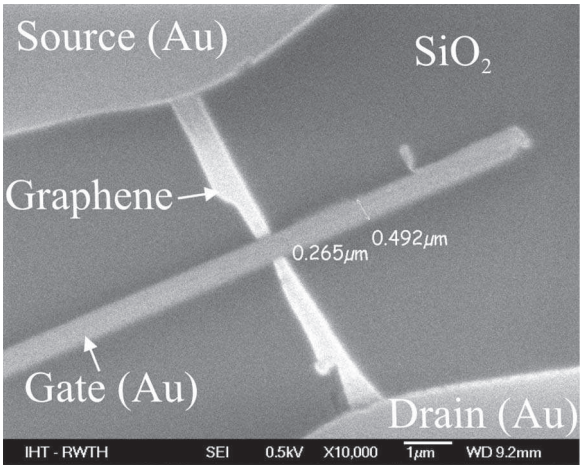

Figure 1.9: An SEM image of the first field effect transistor made from graphene on a SiO_2 substrate with gold leads and a gold gate produced by Lemme in 2007 [32]. This showed for the first time the promise that graphene holds for use in micro-electronics.

frequency of 40 Ghz [37].

The physics of these new devices has drawn the attention of theorists as well. Gava, et al. in 2009 [38] did an *ab initio* study using density functional theory to look at the screening of top and bottom gated graphene bilayers and developed a generalized full band structure for gated graphene. Falkovsky also examined gated bilayer graphene [39], but using a tight-binding model, to find conduction to valence band gap as a function of the strength of the screening constant and the gate voltage.

Understanding how graphene screens is one of the current critical problems being attacked by several groups. Wang and Chakraborty compared the screening in a single layer of graphene to bilayer graphene and showed that the static screening is anisotropic and stronger in the bilayer [40]. Calculations of the dynamical dielectric screening in graphene performed by Hwang and Das Sarma in 2007 showed that the plasmon dispersion at low momentum displays the classical $\omega = \omega_0\sqrt{q}$ frequency

behavior, but the density dependence of the plasma frequency goes as $\omega_0 \propto n^{1/4}$ instead of usual $\omega_0 \propto n^{1/2}$ for a 2D system [41]. Extensive work from Antonio Castro Neto's group at Boston University on the coulomb impurity problem and electron-electron interactions in graphene has been ongoing for several years. Their work concluded that, while the Dirac equation is an excellent model for the low energy system near the K and K' corner, it does leave out several features, such as bound states and renormalization of the van Hove singularities, that are described exactly by using a tight-binding model which includes the lattice [42]. In 2008 they showed that vertex corrections to the polarization bubble have a significant effect on strength of an effective charge in the strong coupling regime [43], and that it is possible to create gapped graphene which has a screening charge that is comparable to the impurity charge [44]. Additionally, in 2009, Polini, et al. [45] demonstrated using density functional theory that the unusual electron-electron interactions in graphene, which cause the exchange and correlation contributions to the chemical potential to increase rather than a decrease as a function of carrier density, increase the ability of the system to screen.

The recent experimental and theoretical work on graphene has had its pitfalls as well as its successes. One of the predictions coming from theoretical work is that the band crossing at Dirac points should become very steep and should show a near divergence in the velocity for a fine structure constant of $\lambda \simeq 2$ [46, 47], where λ is the ratio of the strength of the potential energy to the kinetic energy,

$$\lambda = U/K.$$

However, recent experiments have been unable to verify these predictions; in particular, a huge study in 2008 by Grüneis, et al. [48] compared photoemission spectra to first-principle techniques, which included interactions effects at the level of GW

needed to achieve the exact dispersion, and found that the theory broke down near Fermi level. Other ARPES experiments by Zhou, et al. [49] in 2006 and Bostwick, et al. [50] in 2007 also measured the band crossing in a graphene at the Dirac point.

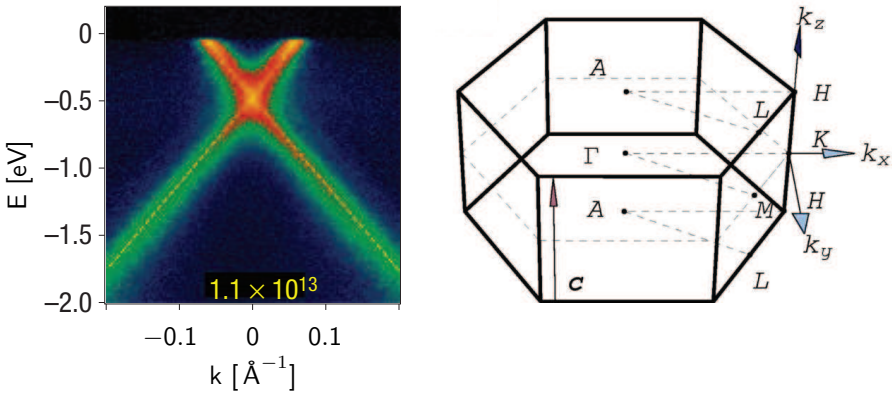

Figure 1.10: **Left:** An ARPES experiment by Bostwick, et al. [50] in 2007 shows the bands of graphene at Dirac point. The dispersion shows no significant deviation from a linear function, in contrast to some theoretical models. **Right:** The first Brillouin zone of a hexagonal honeycomb lattice with major reference points such as K and Γ marked in the figure [51].

Their data showed very straight bands which cross with no anomalous dispersion for momentum parallel to the ΓK direction.

Further evidence contradicting the divergent velocity supposition was presented by a measurement of the inverse density of states by Martin, et al. [52] in 2008. Using a scannable single electron transistor, they were able to measure the inverse compressibility, $\partial\mu/\partial n$, which is equal to the many-body inverse density of states, $1/N(\omega)$. The best fit for the inverse density of states data was that of a non-interacting electron system; e.g.: the standard graphene model has a density of states that rises linearly with momentum around the Dirac points giving way to a $1/p$ (or $1/v$) function for

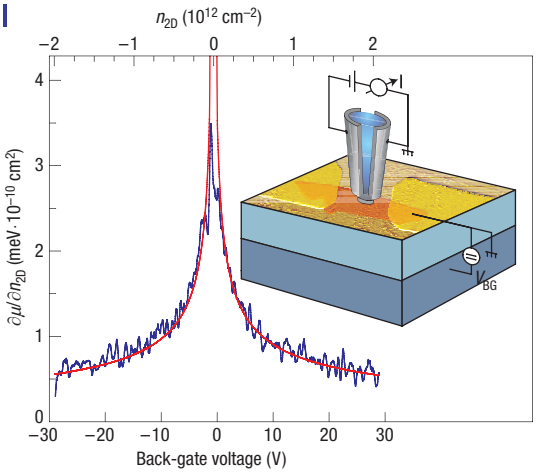

Figure 1.11: A compressibility measurement performed by Martin, et al. [52] in 2008 shows the many-body inverse density of states of graphene around the Dirac point. The data is best fit by a $1/v$ curve indicated a non-interacting picture for the nearby electrons. The inset is a digram of the experimental setup with a single sheet of graphene resting on a doped Si substrate and back gated with a voltage, V_{BG}, to control the carrier density; above the graphene sheet is the scanable single electron transistor which measures the modulation in the local electron density.

the inverse density of states as seen in the Figure 1.11.

We believe the source of this discord comes from an assumption about the electron correlation strength in graphene, λ. For a system of Dirac Fermions with perfect, linear dispersion, this quantity is independent of the electron density and is equal to

$$\lambda = \frac{e^2}{\epsilon\, v_F \hbar}. \tag{1.8}$$

where v_F is the Fermi velocity and ϵ isthe dielectric constant.

The size of the dielectric constant is the likely culprit for causing the discrepancy between theory and experiment. Many groups working on graphene use an assumed value between $\epsilon = 1$ [53, 54, 55] and $\epsilon = 1.75$ [47] for the size of ϵ. By examining

the charge structure of quasiparticles in graphite we attempt to gain insight into the dressing of charges and the weakening of their interactions from which we can obtain the size of ϵ for graphite (which should have a value comparable to graphene). The ability to directly compare measurements on graphite to graphene would be a great contribution to current experimental physics as it would partially circumvent the painstaking process of obtaining and preparing graphene samples.

We have begun preliminary work toward this goal in creating a computational algorithm which converts 3-dimensional loss function data to 2-dimensions based on a few reasonable assumptions. Though the method is still in its infancy, early results are showing promise. In addition to the numerical data processing, we also have expanded the ultra-fast imaging technique created by Abbamonte, et al. [56] to multiple dimensions. This allows us to do two important things: first, we can obtain physical characteristics from the real-space density map of the quasiparticle cloud such as its spatial extent and the symmetry of its shape. And second, we can view with 10 attosecond resolution the dynamical real-space density cloud form and oscillate around the electron as the quasiparticle is born. We also performed convolutions on the dynamical quasiparticle data to test the rigidity of the charge density cloud as the quasiparticle is set in motion. This serves as a test of the validity of the quasiparticle concept as it propagates at different velocities.

However, before any of the aforementioned analysis occurs the data must be collected. We need to sort out how the interactions between particles behave, and for this we need to know the propagator, $\chi(\vec{q}, \omega)$ in equation (1.3). Inelastic X-ray scattering measures precisely this quantity. We use inelastic X-ray scattering to measure nearly the entire energy-loss spectrum over a wide range of momentum and across a large span of frequency (energy) to capture what is happening at very small distances and on a very short time scale. Inelastic x-ray scattering has been used

by condensed matter physicist for about 35 years [57, 58] to obtain the dynamical structure factor, $S(\vec{q}, \omega)$, for various materials. But it was not until scientists began to build end stations at synchrotrons with inelastic x-ray scattering setups in the mid-1980s [59, 60, 61, 62] that the technique began to fully realize its potential.

II Experiment

Measurement Theory

The primary objective of our measurement process is to gather enough data to reliably reconstruct $\chi''(\vec{q},\omega)$, the imaginary part of the density-density Green's function, which is proportional to our data. The events we measure primarily involve the scattering of a photon from an electron (a two photon event) rather than just the absorption or emission of a photon (a one photon event). Building on this concept, we begin with an initial system (electron and photon) state $|\phi_0\,\vec{k}\,\alpha\rangle$, where ϕ_0 is the electron's initial state (not necessarily the ground state) and where $\vec{k}$ and $\vec{\varepsilon}_\alpha$ are the photon's momentum and polarization respectively. If we allow them to scatter to final a random final state $|\phi_n\,\vec{k}'\,\beta\rangle$, then using inelastic X-ray scattering, we can measure the double differential cross section

$$\left(\frac{\mathrm{d}^2\sigma}{\mathrm{d}\Omega\,\mathrm{d}\omega'}\right)_{\vec{k}\alpha\to\vec{k}'\beta} = (k'/k)\left(\frac{e^2}{mc^2}\right)^2 |\,\vec{\varepsilon}^{\,*}_\alpha\cdot\vec{\varepsilon}_\beta\,|^2\times\ S(\vec{q},\omega) \tag{2.1}$$

$$\begin{aligned} S(\vec{q},\omega) &= \sum_{ij}\sum_{n,\phi_0} P_{\phi_0}\langle\phi_0\,|\,\mathrm{e}^{-\mathrm{i}\vec{q}\cdot\vec{r}_i}\,|\,\phi_n\rangle\langle\phi_n\,|\,\mathrm{e}^{\mathrm{i}\vec{q}\cdot\vec{r}_j}\,|\,\phi_0\rangle\ \delta\big(\hbar\,\omega-(E_n-E_0)\big) \\ &= \sum_{n,\phi_0} P_{\phi_0}\langle\phi_0\,|\,\hat{\rho}(\vec{q})\,|\,\phi_n\rangle\langle\phi_n\,|\,\hat{\rho}(-\vec{q})\,|\,\phi_0\rangle\ \delta\big(\hbar\,\omega-(E_n-E_0)\big) \end{aligned} \tag{2.2}$$

where $S(\vec{q},\omega)$, called the dynamical structure factor, has been appropriately summed over the random final states and the thermally distributed initial states of the scattered electron given by

$$P_{\phi_0} = \frac{\mathrm{e}^{-E_{\phi_0}/k_BT}}{\mathbb{Z}} \tag{2.3}$$

where $\mathbb{Z}$ is the canonical partition function. We implicitly made use of the definition of the density, $\hat{\rho}(\vec{r}) = \sum_i \delta(\vec{r}-\vec{r}_i)$, or in momentum space $\hat{\rho}(\vec{q}) = \sum_i \mathrm{e}^{-\vec{q}\cdot\vec{r}_i}$. Moreover, we also apply the standard definitions for $\vec{q}$ and ω of $\vec{q}=\vec{k}-\vec{k}'$ and $\hbar\,\omega = E_k - E_{k'}$ where k and k' are the initial and final momentum states of the photon.

Accordingly, collection of IXS data gives a measurement of $S(\vec{q},\omega)$, while we would like to measure $\chi''(\vec{q},\omega)$. Luckily, $\chi''(\vec{q},\omega)$ is related to $S(\vec{q},\omega)$ through Linear Response theory and the Fluctuation-Dissipation theorem. We start by taking a result from Linear Response theory, the linear response function

$$\chi(\vec{r},\vec{r}';t-t') = \frac{\text{-}i}{\hbar}\langle\phi_0\,|\,[\hat{\rho}_I(\vec{r},t),\hat{\rho}_I(\vec{r}',t')]\,|\,\phi_0\rangle\cdot\boldsymbol{\Theta}(t-t') \tag{2.4}$$

where $\hat{\rho}_I(\vec{r}',t')$ is the density operator in the interaction picture. This quantity describes how the electron density at given point $\vec{r}$ and time t responds to an external potential applied to the electron density at $\vec{r}'$ and time t'. We assume translational invariance and take the Fourier transform over space and time to get

$$\chi(\vec{q},\omega) = \frac{\text{-}i}{\hbar}\frac{1}{V}\int \mathrm{d}\vec{r}\,\mathrm{d}\vec{r}'\mathrm{e}^{-i\vec{q}\cdot(\vec{r}-\vec{r}')}\int_{-\infty}^{\infty}\mathrm{d}t''\mathrm{e}^{-i\omega t''}\;\chi(\vec{r},\vec{r}';t''), \tag{2.5}$$

where $t'' = t - t'$. Solving this integral requires inserting a complete set of states, $\sum_n |\,\phi_n\rangle\langle\phi_n\,| = 1$, into the commutator within the definition of $\chi(\vec{q},\omega)$,

$$\left[\hat{\rho}_I(\vec{r},t),\Big(\sum_n |\,\phi_n\rangle\langle\phi_n\,|\,\Big)\hat{\rho}_I(\vec{r}',t')\right], \tag{2.6}$$

and recalling that we can define an interaction picture operator in terms of a Schrödinger operator as $\hat{\rho}_I = \mathrm{e}^{i\hat{H}t}\,\hat{\rho}\,\mathrm{e}^{-i\hat{H}t}$, and $\mathrm{e}^{-i\hat{H}t}\,|\,\phi_n\rangle = \mathrm{e}^{-iE_nt}\,|\,\phi_n\rangle$, which yields

$$\begin{aligned}\chi(\vec{q},\omega) = \frac{1}{\hbar}\sum_n\Bigg[&\frac{\langle\phi_0\,|\,\hat{\rho}(\vec{q})\,|\,\phi_n\rangle\langle\phi_n\,|\,\hat{\rho}(-\vec{q})\,|\,\phi_0\rangle}{\hbar\,\omega-(E_n-E_0)+i\eta}\\ &-\frac{\langle\phi_0\,|\,\hat{\rho}(-\vec{q})\,|\,\phi_n\rangle\langle\phi_n\,|\,\hat{\rho}(\vec{q})\,|\,\phi_0\rangle}{\hbar\,\omega+(E_n-E_0)+i\eta}\Bigg].\end{aligned} \tag{2.7}$$

The electron density must be a real function, so the relation $\hat{\rho}(-\vec{q}) = \hat{\rho}^\dagger(\vec{q})$ holds, enabling us to write $\langle\phi_0\,|\,\hat{\rho}(\vec{q})\,|\,\phi_n\rangle\langle\phi_n\,|\,\hat{\rho}(\text{-}\vec{q})\,|\,\phi_0\rangle = |\langle\phi_n\,|\,\hat{\rho}^\dagger(\vec{q})\,|\,\phi_0\rangle|^2$. Taking the imaginary part of both sides of equation (2.7) and applying the identity

$\mathrm{Im}\Big[\lim_{\eta\to 0}(\alpha+i\eta)^{-1}\Big] = \text{-}\pi\,\delta(\alpha)$ we get

$$\mathrm{Im}\big[\chi(\vec{q},\omega)\big] = \frac{\text{-}\pi}{\hbar}\sum_n \Big\{ |\langle\phi_n|\,\hat{\rho}^\dagger(\vec{q})\,|\phi_0\rangle|^2\;\delta\big(\hbar\omega-(E_n-E_0)\big) - |\langle\phi_n|\,\hat{\rho}(\vec{q})\,|\phi_0\rangle|^2\;\delta\big(\hbar\omega+(E_n-E_0)\big)\Big\}. \tag{2.8}$$

To finally link the dynamical structure factor and the density-density correlation function we rewrite our expression for $S(\vec{q},\omega)$ at zero temperature from equation (2.2) as

$$\begin{aligned} S^{(0)}(\vec{q},\omega) &= \sum_n \langle\phi_0|\,\hat{\rho}(\vec{q})\,|\phi_n\rangle\langle\phi_n|\,\hat{\rho}(-\vec{q})\,|\phi_0\rangle\;\delta\big(\hbar\omega-(E_n-E_0)\big) \\ &= \sum_n |\langle\phi_n|\,\hat{\rho}^\dagger(\vec{q})\,|\phi_0\rangle|^2\;\delta\big(\hbar\omega-(E_n-E_0)\big) \end{aligned} \tag{2.9}$$

and notice right away that we can express $\chi''(\vec{q},\omega) = \mathrm{Im}\big[\chi(\vec{q},\omega)\big]$ by solving equation (2.8) with equation (2.9) to get

$$\chi''(\vec{q},\omega) = \frac{\text{-}\pi}{\hbar}\Big(S^{(0)}(\vec{q},\omega) - S^{(0)}(\vec{q},\text{-}\omega)\Big). \tag{2.10}$$

Equation (2.10) is just a statement of the quantum mechanical version of the Fluctuation-Dissipation theorem. Although we have derived this at $T = 0$, the Fluctuation-Dissipation theorem can easily be extended to finite temperature as well. If we include the thermal average of an operator,

$$\langle\hat{A}\rangle_T = \frac{\mathrm{Tr}\Big(\mathrm{e}^{-\hat{H}/k_BT}\,\hat{A}\Big)}{\mathrm{Tr}\Big(\mathrm{e}^{-\hat{H}/k_BT}\Big)} \tag{2.11}$$

to the derivation above, we end up with a Boltzmann factor inserted into equation (2.9) which will result in the finite temperature Fluctuation-Dissipation theorem:

$$\chi''(\vec{q},\omega) = \frac{\text{-}\pi}{\hbar}\left(1-\mathrm{e}^{\frac{\text{-}\hbar\omega}{k_BT}}\right)S(\vec{q},\omega). \tag{2.12}$$

To put some numbers on the temperature dependence we perform our experiment at $T = 300K$ and the energy of our measured plasmons is between $\hbar\omega \approx 7$ eV to 30

eV, which places the prefactor of equation (2.12) at $\left(1 - e^{-30/300k_B}\right) = 1$. Equation (2.12) makes the connection between the measurements we take and the density-density correlation function. How $\chi(\vec{q}, \omega)$ relates to other physical functions such the electron density and dielectric function is described more extensively in the analysis section.

Materials Preparation

We used two separate samples of graphite in our experiment: a superior quality (ZYA grade) highly oriented pyrolytic graphite semi-crystal [63], and a unique single-crystal graphite sample grown in Japan obtained from Y. Cai [64] of Brookhaven National Laboratory. The highly oriented pyrolytic graphite (HOPG) sample is mechanically

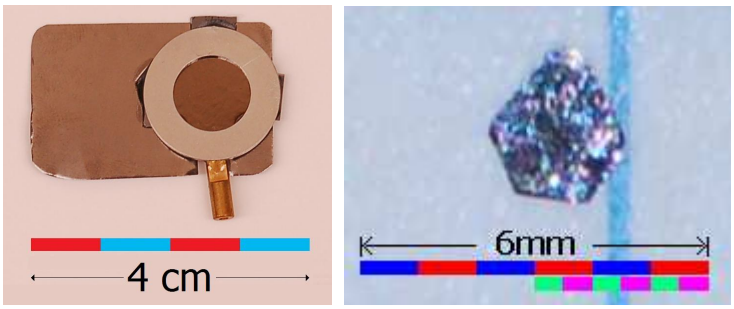

Figure 2.12: Images of our HOPG (left) and SCG (right) samples. The single crystal sample is shown unmounted.

cleaved parallel to the basal planes using a razor blade to separate the crystal into two thinner pieces. The surface of the HOPG sample is then exfoliated using clear plastic tape to smooth and remove any broken layers from the surface. We adhered a metalic washer to the HOPG using epoxy to act as a support and mounting structure. A tantalum sheet with a circular aperture is then glued to the washer to act as a scatter guard against X-rays scattered from the upstream Kapton window of the sample chamber (see below).

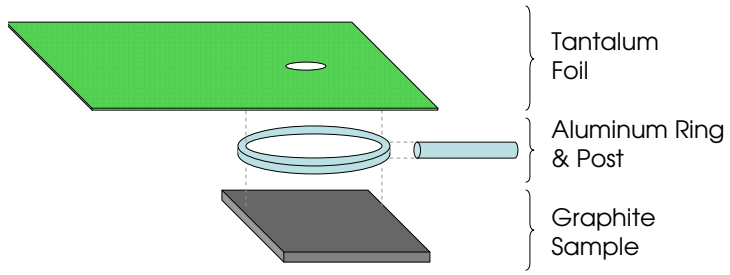

Figure 2.13: Layering of the HOPG sample, support, and Tantalum scatter guard.

The single crystal graphite sample is much smaller than the HOPG sample and therefore was prepared in a different manner. Due to the very minute size (approximately 2 mm wide) of the sample, a mounting support is not necessary. Instead, we used the tantalum scatter guard itself as the base on which the SCG was mounted. We trimmed the tantalum sheet to 1.5 cm by 3.0 cm and punctured a small aperture hole (smaller than the SCG sample) near the bottom. A very thin layer of mild adhesive (rubber cement) is applied to the area surrounding the aperture and any adhesive covering the aperture is removed using a needle tip. We use vacuum tweezers to gently lift and place the single crystal sample over the hole with the aid of an optical microscope. A mounting post is then glued to the scatter guard to allow us to situate the sample on the goniometer.

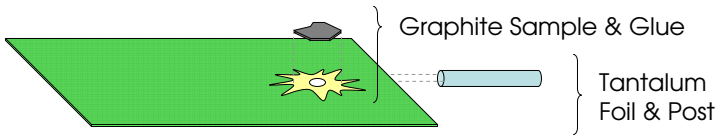

Figure 2.14: The small single crystal sample gets mounted directly over a hole on the Tantalum scatter guard due to its very small and fragile size.

Both of the graphite samples make use of a tantalum scatter guard. The purpose of the scatter guard is to block stray X-rays that have scattered from the upstream Kapton window from reaching the analyzer. We chose tantalum because it strongly attenuates X-rays around 9 keV and because it is easy to work with and rigid enough to support a small sample (as opposed to lead, which is quite flimsy). The samples are mounted on a small goniometer that resides inside of a 4 inch vacuum canister. The shape of the large vacuum canister prevents normal rotation around the χ direction so the internal goniometer was necessary for scanning along different vectors in the basal plane. Also inside the vacuum canister is a specialized in-situ mobile beam stop. We constructed the beam stop by attaching a rotary piezo-electric motor device called an attocube to the back face plate of the vacuum canister. The attocube's rotation is actuated by electrical signals from the controller which are relayed via feed-throughs in the canister wall. We attached a stainless steel arm with lead tape to the attocube to act as a beam stop for the direct beam that does not get scattered by the sample. This unique device allows us pursue data acquisition at very low scattering angles.

Inelastic X-Ray Scattering

Inelastic X-ray scattering (IXS) is our measurement method of choice for probing the electronic structure of our graphite samples. The X-rays are produced when electrons in the storage ring are passed between a long series of paired alternating magnetic poles called an undulator. The alternating magnetic field causes the electrons to accelerate laterally which in turn forces them to radiate. This forward spray of X-rays called the white beam has angular divergence of approximately 16 μrad in the vertical direction (after passing through a 0.4 mm premonochromator slit gap) and a broad wavelength range with a total flux of approximately 5×10^{14} photons/sec (at 100 mA storage ring current). It impinges upon a Silicon (333) two bounce primary

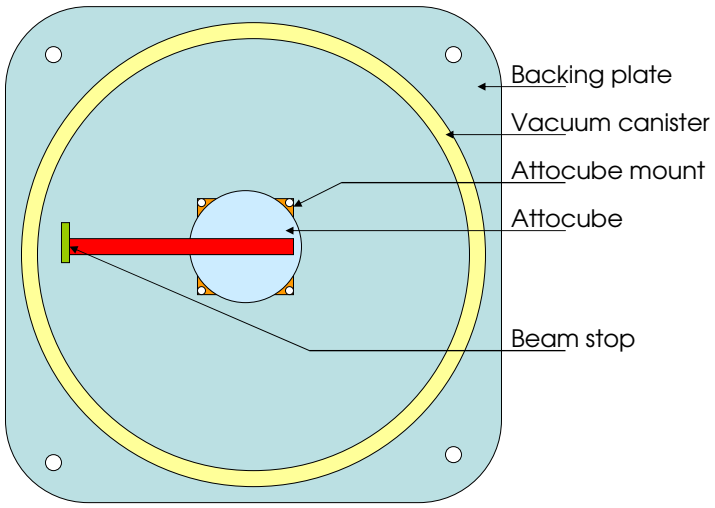

Figure 2.15: The mobile beam stop can be rotated using the attocube while the beam is on. This gives us the great advantage of being able to speed up the data taking process at low $\vec{q}$ by not needing to repeatedly correct a manual beam stop.

monochromator controlled by a Kohzu rotation stage which narrows the beam, drastically reduces the outgoing wavelength range, and greatly increases the resolution, but at the cost of intensity (for even better resolution a secondary monochromator can be placed after the primary monochromator). A piezoelectric motor attached to the second crystal of the primary monochromator controls the vertical position of the beam while the horizontal position is controlled by a rotation of the entire monochromator stage.

Further downstream the beam is reflected off two Rhodium focusing mirrors (one vertical and one horizontal) and then passes through a diagonally split ion chamber. The difference in voltage between the halves of the ion chamber is used as a measure of the beam position. This voltage difference signals a controller in a feedback loop that adjusts the vertical position of the beam via the piezoelectric motor. Beyond

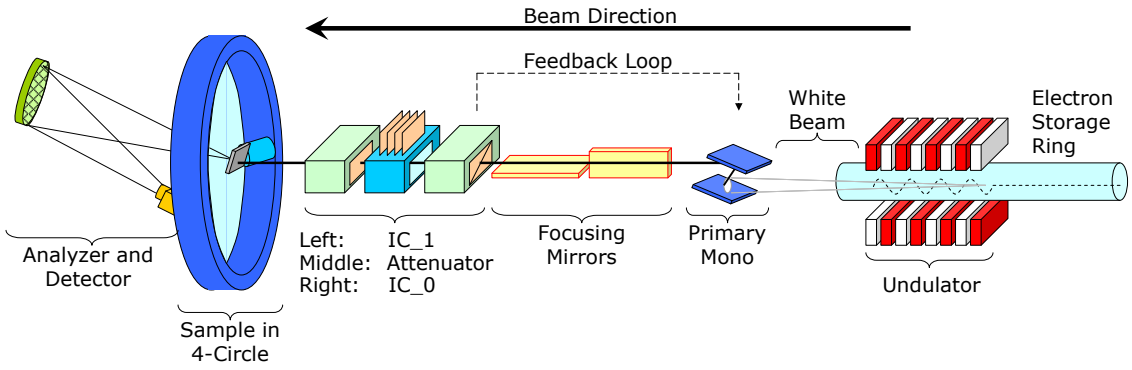

Figure 2.16: A layout of the Inelastic X-ray Scattering process as discussed above. The beam travels from right to left.

the first ion chamber the beam is passed through an array of manually controlled beam attenuators and a second ion chamber which is used for normalization before finally arriving at the sample.

Our sample is mounted in transmission geometry on a small goniometer inside of a vacuum canister in the center of a Huber four-circle diffractometer on a rotation/translation stage. In transmission mode the beam enters the front of the sample, scatters, and then exits through the back (as opposed to reflection geometry where the beam enters and scatter back through the same surface it entered). The intensity of the beam attenuates in a sample of thickness d, entering at an angle of θ, with attenuation length μ, and scattering to an angle tth, by an amount

$$\frac{I}{I_0} = \frac{\mu}{d}\left(\mathrm{e}^{\frac{-d}{\mu\cos\theta}} - \mathrm{e}^{\frac{-d}{\mu\cos tth}}\right)\left(\frac{\cos\theta\,\cos tth}{\cos\theta - \cos tth}\right), \tag{2.13}$$

but we operate under the condition of $tth = 2\theta$ so this simplifies the attenuation to

$$I/I_0 = \mathrm{e}^{\frac{-d}{\mu\cos\theta}}. \tag{2.14}$$

The beam scatters from the sample (into all 4π steradians) and a portion of the scattered X-rays travel through a Helium filled flight path to a 3 inch, spherical,

diced Germanium (733) crystal called the analyzer, which Bragg-reflects the X-rays. The analyzer is mounted 1.0 meter from the sample on a rotary arm and focuses the reflected X-rays back through the Helium filled flight path to an Amptek Si-pin (or Silicon strip) detector set in near-backscattering geometry which collects the counts. We use a near-backscattering geometry to help maintain good energy resolution from the analyzer.

IXS data is measured as a function of two parameters: the momentum imparted to the sample, $\vec{q}$, and the energy injected into the sample, $E = \hbar\omega$. We independently control E and $\vec{q}$ by changing the positions of the primary monochromator's Kohzu motor angle, θ_K, and angle of the analyzer's arm, tth, respectively. The reflected energy of the analyzer is controlled by the d-spacing of its crystal, which in our case was Ge(733) whose backscattering energy is $E_s = 8.9805$ keV. We use the primary monochromator to scan through a range of initial energies, E_i, starting at 8.9805 keV and going up to 200 eV above 8.9805 keV. The difference between the initial and scattered energies gives the energy injected into the sample:

$$\hbar\,\omega = \Delta E = E_i - E_s.$$

Similarly for momentum, the initial beam has momentum, $\vec{k}_i$, and the measured scattered X-ray have average momentum, $\vec{k}_s$. The difference in magnitude is only very slight, small enough that we can confidently make the approximation, $|\vec{k}_i| = |\vec{k}_s| = |\vec{k}|$. This leaves the angle of the analyzer arm as the sole contributor to the difference in the incoming and scattered momentum vectors:

$$\vec{q} = \vec{k}_i - \vec{k}_s$$
$$|\vec{q}| = 2|\vec{k}| \sin\left(\frac{tth}{2}\right).$$

The overall energy resolution of our experiment can be determined by adding in quadrature all of the broadening effects from each of the elements along the flight

path, however it is much easier to simply make a measurement of the resolution after the setup in complete. The full width half max of the elastic peak is what we use as the energy resolution of our experiment, typically around 300 meV. The momentum

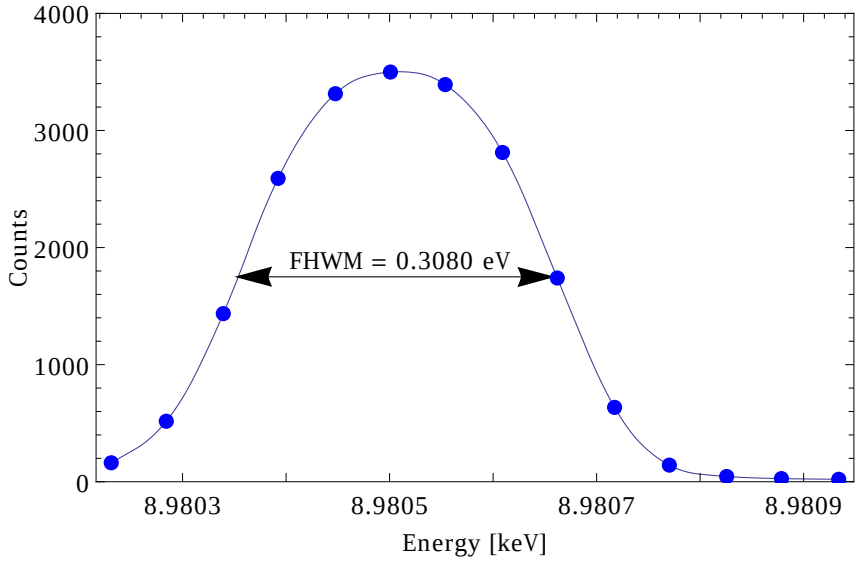

Figure 2.17: An energy scan of the elastic line of HOPG. The full width half max is approximately 300 meV which determines the experimental resolution.

resolution is mostly determined by the combined geometry of the analyzer and the two-theta arm with a slight contribution from energy bandwidth broadening. The momentum resolution occupies a 'pancake' in momentum space which is tilted at an angle according to the angle of the two-theta arm. The projection of the pancake along any of the q_x, q_y, or q_z directions determines the resolution for that direction. We are primarily interested in δq_z, the resolution in the direction of the momentum transfer.

At an energy of 8.9805 keV our momentum resolution is between $\delta q_z = 0.346\,\text{Å}^{-1}$ at our lowest (unmasked) angle of $tth = 8^\circ$ ($\delta q_z = 0.173\,\text{Å}^{-1}$ when masked at $tth = 3^\circ$) and $\delta q_z = 0.173\,\text{Å}^{-1}$ at our highest angle of $tth = 120^\circ$. For the actual data taking

process we stepped tth in increments of 4°, slightly less than the angular opening of the analyzer of 4.36° . Doing so ensures that we do not miss any fraction of data in momentum space and puts our data in increments of the resolution for that angle of tth.

The X-ray detector is the final stop for X-ray in an IXS experiment. We used two different styles of X-ray detectors set in backscattering geometry (where the detector is very close to the sample, at nearly 180° from the analyzer) over the course of our experiment. The vast majority of our data was collected by an Amptek Si-pin model XR100-CR detector with a 150 eV resolution. A very small amount of data was obtained using an Silicon microstrip detector or "strip detector." The strip detector is an array of 1024 silicon 200 micrometer X-ray detectors stacked vertically. Each strip yields and individual readout and the difference in position corresponds to a difference in energy transfer. The advantage is much better resolution and data acquisition at multiple energy losses simultaneously. The disadvantage is lower counts per channel (since they are smaller than the spot detector) and a lower signal to noise ratio. We used strip detector in 'spot mode' with 15 silicon strip channels acting as one collective unit similar to the Si-pin detector. Matching the data from the strip detector to the spot detector was done by simply scaling the scans to previously acquired data at the same momentum.

Alignment and Orientation

Alignment of the diffractometer and orientation of the sample are necessary steps at the beginning of each run. The upstream optics are usually aligned by the local beam line scientists and the energy is set using a Copper film to calibrate the beam energy at the absorption K-edge. To start the alignment process we move the θ and χ motors to their zero positions and place a pin head on the goniometer mounted

to the ϕ motor. We use a telescope to view the pin as we rotate the ϕ stage. By rotating ϕ by 180° and back we check that the center of the pin is aligned along the rotation axis of ϕ.

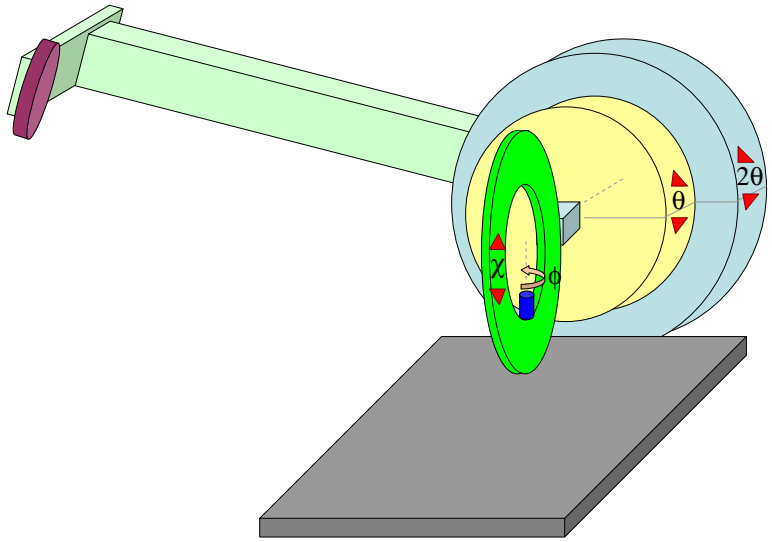

Figure 2.18: The Huber four-circle geometry with the primary angles shown. The entire diffractometer is attached to the translation stage (in gray) which has x, y, z-motion as well as pitch, yaw and roll.

Next, we rotate the χ ring from 0° to 90° and 180°, and use the telescope to place the tip of the pin head in the center of rotation of the χ ring. Now we know that the tip of the pin is in the center of rotation of the diffractometer. Next we attach a piece of burn paper to the pin to find where the beam is passing (if nothing appears on the burn paper we use a large fluorescent screen to find the beam) and move the cross hairs of the telescope to burn spot. Once the telescope is set, it does not move as this gives us our absolute reference whenever needed to find the beam (unless something drastic happens upstream). Now that we have marked the center of rotation with the pin head and the location with the telescope, we slowly adjust the translation stage to bring the pin head into the cross hairs thereby putting the beam directly in the

center of rotation.

The beam is now passing through the center of the diffractometer, but we still need to align all of its appendages. To start we lower the tth arm to 0° and cover the detector with a lead mask (to keep it from being damaged). A fluorescent screen is affixed to the lower half of the analyzer such that its edge lies horizontally along the analyzer's diameter. The beam is turned on and we view its location on the screen via external monitors. We adjust the height of tth so that the screen clips about half of the beam and set the motor position to be zero. We next rotate the entire translation stage to bring the beam spot onto the horizontal center marking on the screen. This puts the center of the analyzer in line with the vertical plane of the beam and sets our $\vec{q} = 0$ position.

The alignment of the analyzer and detector is seemingly the most difficult part of this process. We need to align the position of detector so that it can pick up the X-rays reflected from the analyzer, but we also need to align the angles of the analyzer so it is properly Bragg reflecting back to the detector. Both alignments need to be done simultaneously - an impossible task. Instead, we lower the position of the detector arm motor, $atth$, by 5° and attach a fluorescent screen above it. The tth arm is raised to 20° and a piece of scotch tape is used to scatter the beam. We monitor the fluorescent screen externally while we tweak the positions of the analyzer motors, θ_a and χ_a, until we find the beam spot. We set the analyzer motor angles to those of the Germanium (733) Bragg reflection, $\theta_a = 87.2^{\circ}$ and $\chi_a = 0^{\circ}$, and move the detector back into posistion. To finish the alignment a scan of the detector position, $atth$, finds the maximum of the reflected beam.

Orientation of the sample starts well before we ever set foot on the beam line. After the sample is mounted (either to its metal ring or the Tantalum foil) we use a Phillips X-ray Diffraction system (XRD) to scan the sample and find a Bragg

peak. An XRD system is similar in setup to IXS except it has no analyzer, just an energy-integrating detector. The direction of the Bragg peak angle is marked on the graphite sample's mount as a rough orientation indicator. At the beam line the sample is mounted and oriented by eye to be within 1° of the sample surface being perpendicular to the beam. The ϕ motor is disengaged and we use the telescope to place the sample in the center of rotation by rocking ϕ by 180° and back while making small adjustments on the small goniometer. The ϕ motor is engaged and the small goniometer is adjusted such that χ_{gonio} brings the orientation marking on the Tantalum foil to vertical. At this point the sample is in the center of rotation of the diffractometer, it does not rotate out plane with a change in angle, and the Bragg vector found using XRD is roughly in line with the beam-analyzer-detector plane.

To find the Bragg peak in situ, we do not use the analyzer and detector at all. This is for several reasons: first, Bragg peaks can be very intense and could burn out the detector; second, the analyzer is diced and the Bragg peak sometimes can fall in between the individual crystal elements into a gap; and third, if the χ_{gonio} angle is off by a large amount then the peak would miss the analyzer altogether. Instead we use a very simple low-tech solution of hanging a fluorescent screen behind and above the sample to intercept the Bragg peak. We view the screen with externally controlled cameras as we move the ϕ angle (we use the ϕ motor set at $\chi = 90^{\circ}$ in place of the θ motor) to the approximate desired Bragg condition (i.e.: the (200) reflection) and tweak it until we find the Bragg peak. If needed, χ_{gonio} is adjusted to bring the Bragg peak in-line with the center of the screen and vertical plane of the beam. The ϕ motion is then tweaked through the entire Bragg peak (typically a width of about 1° to 1.4°) and then back until the spot on the screen is at a maximum brightness. We record this angle as ϕ_{high}. The fluorescent screen is lowered to below the sample position and we repeat the above process to find the opposite Bragg condition (the

($\bar{2}00$) reflection) and record the angle as ϕ_{low}. The difference between these two angles is the offset from zero, $|\phi_{high}| - |\phi_{low}| = \phi_{offset}$. We move ϕ to ϕ_{offset} and set ϕ to zero to complete the orientation.

IXS Data

We collected the data over several runs at CMC Sector 9 at the Advanced Photon Source at Argonne National Laboratory. The raw data is in units of counts (N) as a function of energy and the angle tth. Normalizing by the second ion chamber counter and performing some simple arithmetic on the parameters puts our data into its workable form of counts per second (CPS) as a function of energy (eV) and momentum (Å^{-1}). For each scan the momentum parameter (the angles tth and $\theta = tth/2$) is fixed and the primary monochromator energy is scanned across a 200 eV range starting at 0 eV in steps of 0.25 eV, just within our energy resolution. The momentum step size is not in equal increments of a dq; instead we walk the angle tth upward in increasing increments of 4° or less from 3° to 120°. This assures that we have not missed any data in our range of momentum space since the analyzer has an angular opening along tth of 4.36°

For the single crystal graphite sample, the small goniometer mounted inside the vacuum chamber gives us control of the angle of $\vec{q}$ within the sample. We fix the angle of $\vec{q}$, move tth to where we want it, and scan the energy. We repeat this process until we have covered all available angles of $3^{\circ} \leq tth \leq 180^{\circ}$ and energies of $0\,\text{eV} \leq E \leq 200\text{eV}$, at which point we open the hutch, manually change χ_{gonio}, and start the process over.

We compile the scans together to gain a composite view of the electronic excitations for the entire phase space of momentum and frequency $\{q, \omega\}$. The key features in our data are two plasmons: one at low energy and momentum (centered about

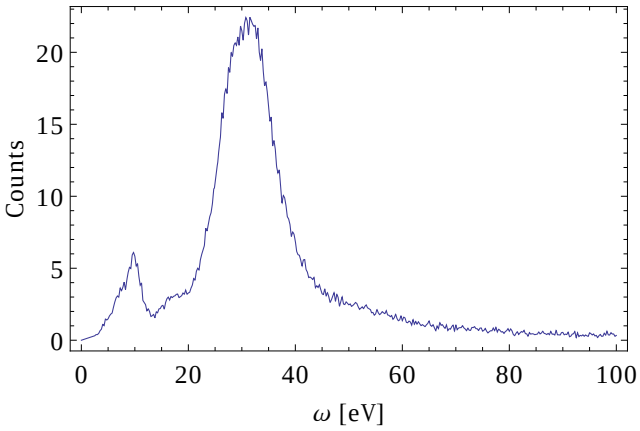

Figure 2.19: A typical single scan of data from our inelastic X-ray scattering experiment with the elastic line removed. The two peaks in the data correspond to plasmon excitations of the π and σ-π plasmons.

13 eV and 1.5 Å^{-1}) coming from the out-of-plane π orbitals, and another a higher energy and momentum (centered about 35 eV and 2.5 Å^{-1}) coming from deeper excitations of the σ-π orbitals, in agreement with other studies [62, 64]. The large feature exhibiting a q^2 dispersion beyond the σ-π plasmon comes from Compton scattering that emerges as we move into the high-q regime. The information that appears beyond 200 eV and 7.88 Å^{-1} comes from the extrapolations discussed in the Analysis section.

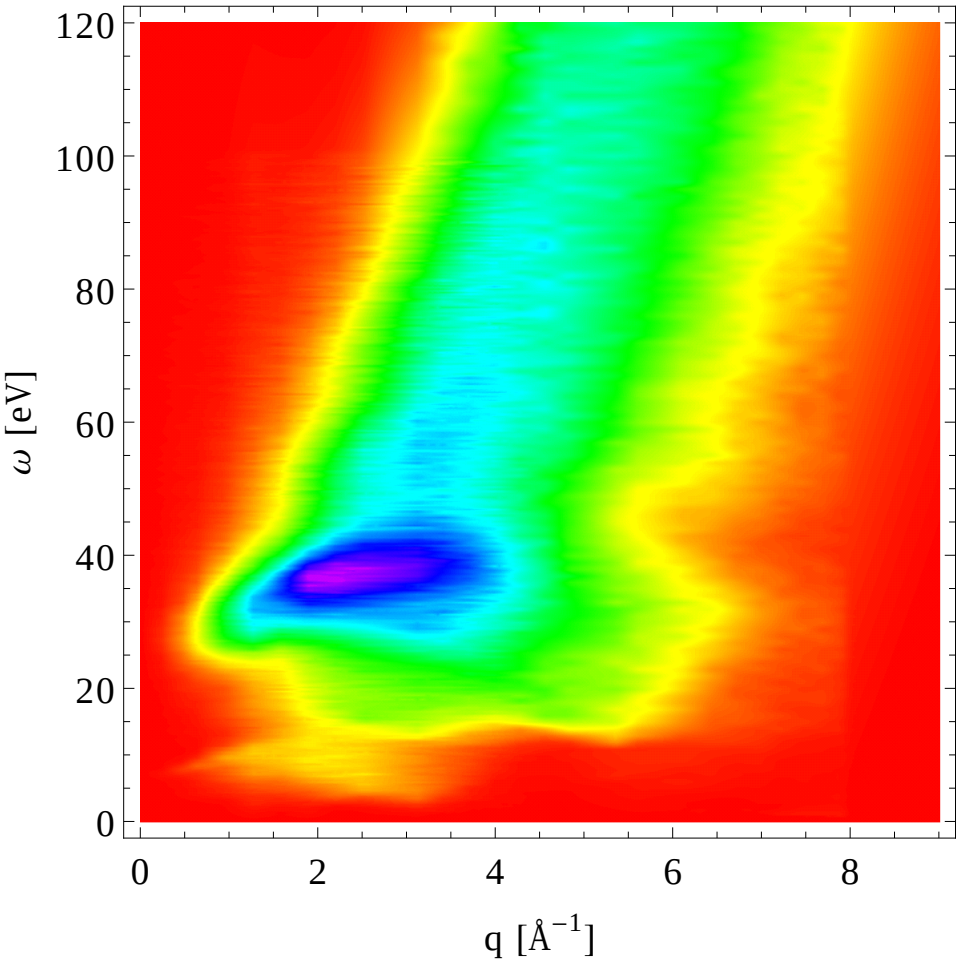

Figure 2.20: A full data set consisting of 28 scans over a 200 eV range. The lower energy and higher energy plasmons arise from excitations between their respective π and σ-π bands. The large upward tail is the Compton scattering regime.

III Analysis

The analysis of the graphite data occurs in two large sections - first we perform the fitting, extrapolation, f-sum rule calculations and scaling on the highly oriented pyrolytic graphite (HOPG) data. Second we use the Kramers-Kronig transformation, Fourier transform, and the Friedel sum rule on the combined HOPG and single crystal graphite (SCG) data. There is a small amount of fitting and scaling on the SCG data before it is merged with the HOPG data.

Highly Oriented Pyrolytic Graphite Data

The data analysis begins by preparing the raw highly oriented pyrolytic graphite data into a usable, comparable form. To start, we normalize the data for two effects (three effects in the case of very low angle data): the total amount of radiation that hits the sample and volume filling effects. The data at each parameter point, $\{q, \omega\}$, is divided by the counts from the ion chamber and subsequently multiplied by a nominal value, in essence normalizing each data point such that the measurements were all performed at the same beam intensity. The volume filling effects are a result of more sample volume being illuminated by the beam as the angle of the sample is increased as in equation (2.14). We remove this effect by dividing by

$$V_{correction}(\theta) = d\, \mathrm{e}^{\frac{-d}{\mu \cos\theta}} \tag{3.1}$$

where d, μ, and θ are the sample thickness, attenuation length at 9 keV, and tilt of the sample, respectively. For the HOPG, the sample thickness is approximately $d = 1500\mu$m, and for the single crystal sample the thickness is approximately $d = 250\mu$m. The attenuation length of X-rays at 8.980 keV in graphite is $\mu = 1485\mu$m.

The next step is the removal of the elastic peak and extrapolation of the data to high energy. The elastic peaks' tails are too wide to be fit to a Gaussian, but the

shape of the peak is too sharp to be fit to a Lorentzian, hence we use a Voigt function (a convolution of a Lorentzian with a Gaussian) to find a good fit,

$$F_{Voigt}(\omega) = y_0 + A\,\frac{2\ln 2}{\pi^{3/2}}\,\frac{w_L}{w_G^2}\int_{-\infty}^{\infty}\frac{\mathrm{e}^{-t^2}}{\left(\sqrt{\ln 2}\,\dfrac{w_L}{w_G}\right)^2 + \left(\sqrt{4\ln 2}\,\dfrac{\omega-\omega_0}{w_G} - t\right)^2}\,dt \qquad (3.2)$$

where w_L and w_G are the width parameters of the Lorentzian and the Gaussian in the convolution. We fit the elastic line at $\omega = 0$ eV to a Voigt function with zero y-offset and then subtract it from the entire scan (we use $y_0 = 0$ for out Voigt fit to prevent out data from going negative upon subtraction where our signal was zero). A typical scan has an elastic peak that is less than 0.3 eV wide at its full wide half max but the shoulders can extend as high as 2 to 3 eV.

The extrapolation of the scans' tails to high energy is necessary to properly apply a Kramers-Kronig transformation at a later stage of the analysis. The extrapolation is performed using a minimized chi-squared fit of each scan of a Gaussian curve to the highest 30 eV to 70 eV. We attach the Gaussian fit piece-wise to the end of each scan to extend the range past 200 eV.

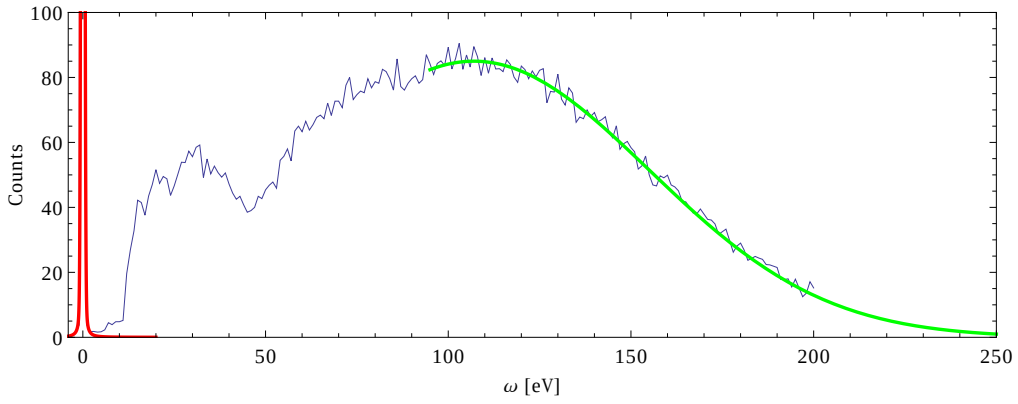

Figure 3.21: An unscaled scan of HOPG at 72° in two-theta. The red curve (left side) is a Voigt function fit to the elastic peak which gets subtracted. The green curve (right side) is a Gaussian to the tail used for extrapolation beyond 200 eV.

We employ several innovative methods to make data acquisition at very low q possible: a movable beam stop, a sample-mounted scatter guard, and a stainless steel mask to reduce the analyzer's solid angle. The first two work by blocking stray photons from entering our detector, thereby improving our signal to noise ratio. The analyzer mask used at low q truncates the available area of the analyzer allowing us to scan at much lower angles. However, the count rate reduction effect must be removed to get a proper comparison among scans. To compensate, the data collected when the mask is used is multiplied by the ratio of the areas, A_{full}/A_{masked}, of the unmasked to masked analyzer. Unfortunately, at the lowest momentum measurement, 3° in two-theta, our data picks up a small amount of background caused by scattering from the vacuum chamber windows. While this does not make the scan completely useless, it does preclude it from being used in the sum rule calculations.

On the other side of the coin, going to very high q reveals a completely different challenge: the rise of a Compton profile. Beginning around $5\,\text{Å}^{-1}$, the plasmons start to reside on the back of a large 'hill' in the data, the emergence of the Compton scattering regime. At $7.88\,\text{Å}^{-1}$, the highest momentum we measured, the data consists entirely of Compton scattering peaked at $\hbar^2q^2/2m$ with no other significant features.

The nature of Compton profiling is such that the energy dependence of the data is normally removed leaving the data as a function of the projection of the electron momentum in the sample, $\mathsf{z} = p_0 \cos\phi$, which is independent of the experimental setup. Conservation of energy and momentum in the Compton scattering process gives a relation between the scattered photon energy, $\hbar\omega$, and the projection of the initial momentum of the electron as

$$\hbar\omega = \frac{\hbar^2 q^2}{2m} + \frac{\hbar\, q\, \mathsf{z}}{m} \tag{3.3}$$

where m is the mass of the electron [65]. The first term on the right is the Compton

shift due to scatter from an electron at rest while the second term is a Doppler broadening around the Compton shift due to the motion of the electrons in the sample. Isolating z gives

$$\frac{\hbar}{m}\mathsf{z} = \frac{1}{q}\left(\hbar\omega - \frac{\hbar^2 q^2}{2m}\right) \tag{3.4}$$

for the distribution of the projected electron momentum. Realizing that the distribution of z will be the same over a large range of momenta allows us to use equation (3.4) to shift and spread the entire profile via

$$\frac{1}{q'}\left(\hbar\omega' - \frac{\hbar^2 q'^2}{2m}\right) = \frac{\hbar\mathsf{z}}{m} = \frac{1}{q}\left(\hbar\omega - \frac{\hbar^2 q^2}{2m}\right) \tag{3.5}$$

$$\hbar\omega' = \frac{q'}{q}\left(\hbar\omega - \frac{\hbar^2 q^2}{2m}\right) + \frac{\hbar^2 q'^2}{2m}. \tag{3.6}$$

Equation (3.6) allows us to shift the Compton profile taken at momentum q with data points at ω to q' and ω'.

To extrapolate beyond $7.88\,\text{Å}^{-1}$ we begin by fitting the Compton profile to a Gaussian,

$$G_{fit}(\omega) = A\left(\mathrm{e}^{-\hbar^2(\omega-\omega_0)^2/2\sigma^2} - \mathrm{e}^{-\hbar^2(\omega+\omega_0)^2/2\sigma^2}\right) \tag{3.7}$$

where $\omega_0 = \hbar\,(7.88)^2/2m$ and A and σ are fit parameters. To extend the $G_{fit}(\omega)$ to higher momentum, we plug equation (3.6) into equation (3.7) to get

$$F_{Compton}(q,\omega) = \left(\frac{7.88}{q}\right) G_{fit}\big(\,\omega_{shift}(q,\omega)\,\big), \quad q > 7.88 \tag{3.8}$$

$$\omega_{shift}(q,\omega) = \frac{7.88}{q}\left(\omega - \frac{\hbar^2 q^2}{2m}\right) + \frac{\hbar^2\,7.88^2}{2m}. \tag{3.9}$$

The Compton profile function is normalized by $7.88/q$ to account for the Jacobian of the transformation. This Compton extension ends up being superfluous since it gets suppressed when the entire data set is divided by q^2 when converting to density at a later point in the calculation.

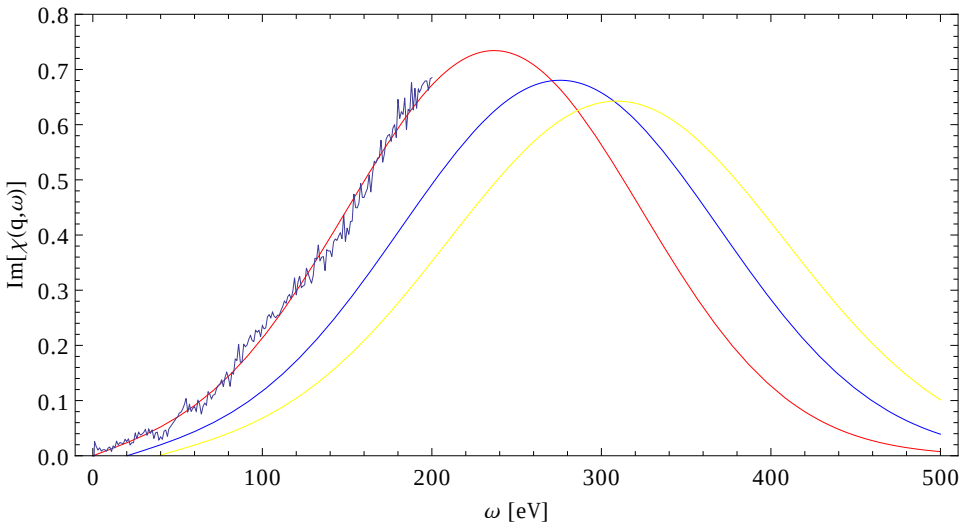

Figure 3.22: A scaled scan of HOPG at our highest momentum, $q = 7.88\,\text{Å}^{-1}$. The data at this large of momentum is nearly entirely Compton scattering. The data is fit with a Gaussian (leftmost curve) whose peak resides at $\hbar^2 q^2/2m$. This fit is then used to extrapolate to higher momentum as shown in the blue (middle) and yellow (rightmost) curves ($8.5\,\text{Å}^{-1}$ and $9.0\,\text{Å}^{-1}$ respectively).

Once the data is compiled with the elastic lines removed, the high energy tails extended and the Compton profile extrapolated into a complete data set, $\mathsf{D}(\vec{q},\omega)$, we set it to an absolute scale using the f-sum (Thomas-Reiche-Kuhn) rule,

$$\int_{-\infty}^{\infty} \omega \left(-\text{Im}\left[\frac{1}{\epsilon(\vec{q},\omega)}\right] \right) d\omega = \omega_p^2, \tag{3.10}$$

$$\text{Im}\left[\frac{1}{\epsilon(\vec{q},\omega)}\right] = \text{Im}\left[\frac{4\pi e^2}{q^2}\chi(\vec{q},\omega)\right] \tag{3.11}$$

$$\omega_p = \sqrt{\frac{4\pi\, n\, e^2}{m}} \tag{3.12}$$

where n and m are the electron density and mass. This rescales it from units of counts per second (CPS) to the density-density Green's function,

$$\chi(\vec{q},\omega) = \frac{\text{-}i}{\hbar}\frac{1}{V}\int \text{d}\vec{r}\,\text{d}\vec{r}\,' \text{e}^{-i\vec{q}\cdot(\vec{r}-\vec{r}\,')} \int_{-\infty}^{\infty} \text{d}t'' \text{e}^{-i\omega t''}\ \chi(\vec{r},\vec{r}\,';t''), \tag{3.13}$$

with units of $(\text{eV} \cdot \text{asec}^3)$. The scaling factors calculated from the sum rule at each of the lower q values are averaged to obtain an overall scaling constant for converting the data. The electron density, n, is calculated simply as the number of electrons

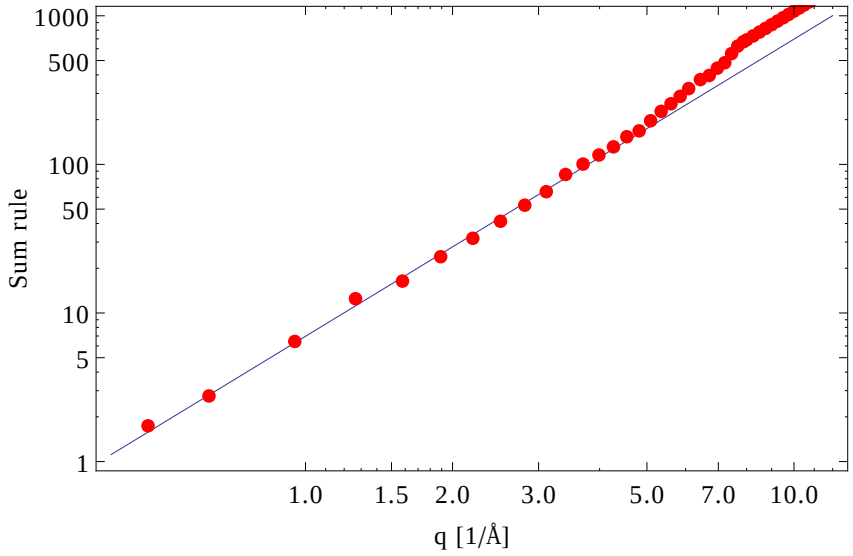

Figure 3.23: A log-log plot of the left and right hand side of the sum rule for the imaginary part of $\chi(\vec{q}, \omega)$. The sum rule on χ scales with q^2 as shown in the image (as opposed to $1/\epsilon$ which is independent of q). The red point plot is the data scaled to the sum rule. The purple line is the right hand side of the sum rule as a function of q for $n = 4$ electrons. At around $5\,\text{Å}^{-1}$ Compton scattering starts to become prevalent in the spectrum, which will include the deeper $1s$ electrons normally left out of the calculation. The addition of these extra 2 electrons cause the integral (dots) to diverge from the their theoretical value (line).

per unit cell volume in graphite under that assumption that only the four electrons in $2p$ and $2s$ orbitals participate in the excitations seen in the spectrum. As seen in Figure 3.23 this assumption holds true up to about $5\,\text{Å}^{-1}$, beyond which the much deeper $1s$ electrons are excited into Compton spectrum which throws off the sum rule

calculation at higher momentum.

Single Crystal Graphite Data

From the single crystal graphite we measured six sets of data, identical in q and ω to the HOPG data, at increments of six degrees in ψ from the (100) direction to the (110) direction. Comparison of the peak positions, shape, and height of the π plasmon at each angle ψ and fixed $|\vec{q}|$ value showed distinct anisotropy in the π plasmon from $0.9\,\text{Å}^{-1}$ to $2.2\,\text{Å}^{-1}$ in momentum and from 0 eV to 15 eV in energy. However, the

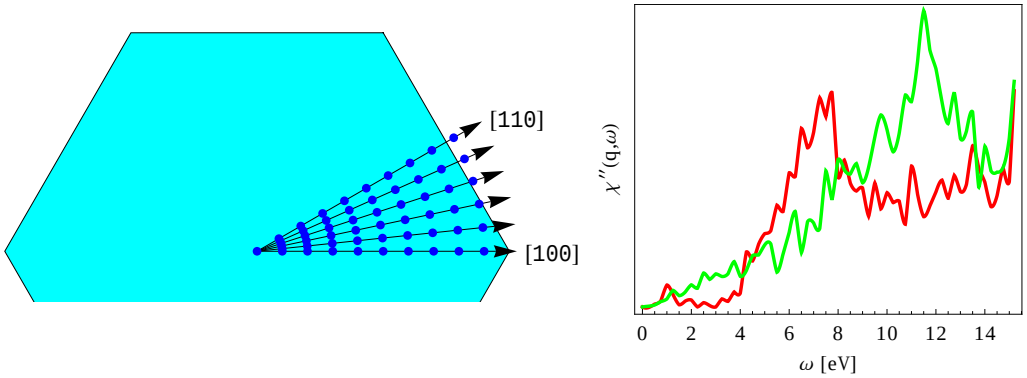

Figure 3.24: **Left:** The blue dots are a generalized representation of the various $\vec{q}$ values at which data was taken from the single crystal graphite sample. Data was taken along six equal spaced angles in ψ in the 30° wedge between the (100) and (110) directions. **Right:** The overlaid scans are both taken at $|\vec{q}| = 1.7\,\text{Å}^{-1}$. The red scan was taken at $\psi = 0^{\circ}$ along the (100) direction, while the green scan was taken at $\psi = 30^{\circ}$ along the (110) direction. The anisotropy is evident in the height, shape, and center of the π plasmon peak.

single crystal data at higher energy (above 15 eV), specifically the σ-π plasmon, lacks any clear anisotropy within our experimental resolution when comparing: scans at one ψ value to another ψ value (at the same momentuma), a single scan at any ψ

versus the average of the scans across all six ψ angles, or a single scan at any ψ against the HOPG data. This leaves a finite window of single crystal data that significantly differs from the HOPG data. This is not entirely unexpected since as either $\vec{q}$ or E goes to zero the data along all directions must be single-valued. Moreover, as $\vec{q}$ becomes large the electrons begin to form a Compton profile in which anisotropies of the valence electrons are minute and can only be seen in difference profiles taken at extremely high momentum [66]. Thus, we expect our use of HOPG data, which has better statistics and less noise for the small and large momentum ranges, to be rather reasonable. We will use HOPG data for the low q and high q sections above 15 eV; elsewhere we will incorporate single crystal graphite data.

Incorporation of the single crystal graphite data into the scaled HOPG data starts by dividing each scan of SCG data by the counts from the ion chamber monitor to remove any beam effects from the data. We then scale the average of the six single crystal scans at each momentum, $|\vec{q}|$, to the HOPG data using a simple chi-squared minimization from 0 eV to 15 eV, the range of the π plasmon. The average is used to scale the SCG scans to preserve the differences in height of the peaks in the single crystal data (as opposed to scaling each scan individually to the HOPG data). The scaled and combined SCG and HOPG data creates a 30° slice of the anisotropic density-density Green's function, $\mathrm{Im}[\chi(q,\omega,\psi)] = \chi''(q,\omega,\psi)$. By repeatedly folding this wedge over the appropriate symmetry axes we replicate the data, giving the complete $\chi''(\vec{q},\omega)$ for any momentum direction, $\vec{q} = (q\cos\psi, q\sin\psi, 0)$, in the entire basal plane.

Computation

After the full compilation (HOPG, SCG and Compton) of $\chi''(\vec{q},\omega)$ is completed we move on to the second stage of the analysis. The ultimate goal is to view the

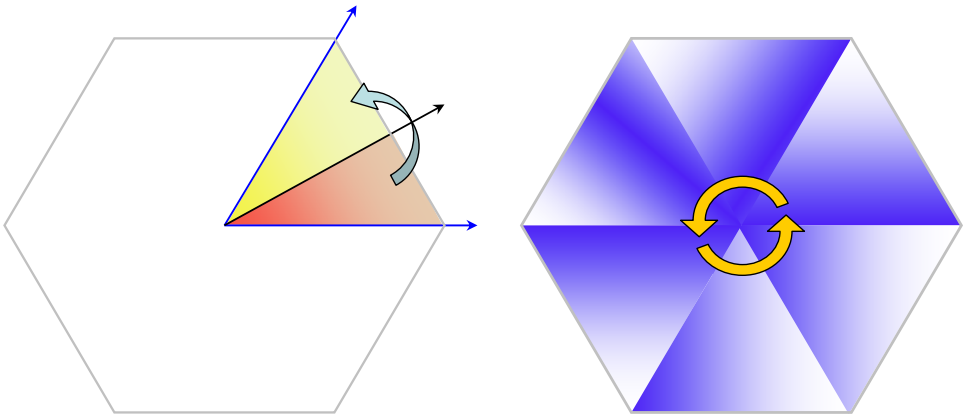

Figure 3.25: **Left:** The initial replication of the 30° data wedge (red sector) by folding over the (110) axis, indicated as the black arrow. **Right:** The Brillouin zone of graphite is six-fold symmetric with each of the six sectors being identical to the newly formed 60° wedge of data. This allows us to construct a full set of data for any point of the Basal plane.

electron density modulation in space and time, $\rho(\vec{r},t)$, starting from $\chi''(\vec{q},\omega)$, given the relation

$$\rho(\vec{q},\omega) = -e\,V(\vec{q})\,\chi(\vec{q},\omega) \tag{3.14}$$

where $V(\vec{q}) = \frac{4\pi e^2}{q^2}$ for a 3-dimensional system. We use $e = -1$ for the charge and begin by calculating

$$\mathrm{Im}[\Sigma(\vec{q},\omega)] = \frac{4\pi e^2}{q^2}\chi''(\vec{q},\omega) \tag{3.15}$$

before the data is linearly interpolated to avoid anomalies that come from division by q^2 at low q. $\mathrm{Im}[\Sigma(\vec{q},\omega)]$ is the density point-data at each value of the measured values of $\vec{q}$ and ω. To handle the pole at $q = 0$ we simply copy the value of $\mathrm{Im}[\Sigma(\vec{q},\omega)]$ at our lowest measured q value. Since $\mathrm{Im}[\Sigma(\vec{q},\omega)]$ already has the division by q^2, this extrapolation to $q = 0$ avoids the issue of the pole completely. The division by q^2 at this point in the calculation also suppresses the Compton profile by such a large

factor that the extrapolation we performed in the previous portion of the analysis becomes nearly extraneous.

Each of the data points of $\mathrm{Im}[\Sigma(\vec{q},\omega)]$ is connected linearly to every surrounding point in its parameter space creating a piece-wise function of line segments which represent the imaginary part of the density in momentum-frequency space, $\mathrm{Im}[\rho(\vec{q},\omega)]$. We use a linear interpolation instead of a squared or cubed function to be as honest with the data as possible - i.e. we don't want to add a local maxima or minima where we don't know one exists.

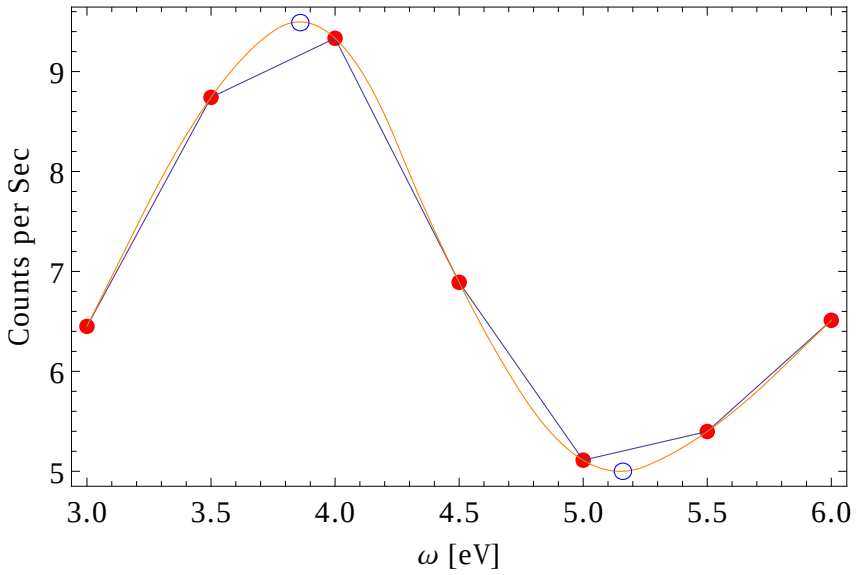

Figure 3.26: Two examples of data interpolation. The data points (red circles) are connected by using both a linear (straight) and quadratic (curved) functions above. The quadratic interpolation adds extrema (indicated by the open blue circles) where we do not absolutely know there should be.

Statics

The cloud of electrons surrounding the impurity screens the test charge, greatly reducing the strength of its Coulomb interaction. The electron cloud and the charge

together form a quasiparticle of the graphite system: a Fermion with a Yukawa potential that weakly interacts with the other charges in the system allowing graphite to have rigid, well-defined bands and its distinct Fermi surface.

To examine the steady state electron density distribution we look at the infinite time component of the electronic density, $\rho(\vec{q}, t{=}\infty)$, requires knowledge of $\rho(\vec{q}, \omega)$ at $\omega{=}0$. However, due to the nature of the Green's function, the imaginary part $\mathrm{Im}[\rho(\vec{q}, \omega)]$ is zero at $\omega{=}0$. Therefore, we make use of the Kramers-Kronig transformation

$$\chi'(\vec{q}, \omega) = \frac{2}{\pi}\,\mathcal{P}\!\int_0^\infty \frac{\omega' \cdot \chi''(\vec{q}, \omega')}{\omega'^2 - \omega^2}\, d\omega' \tag{3.16}$$

to obtain $\mathrm{Re}[\chi(\vec{q}, 0)] = \chi'(\vec{q}, 0) = \chi(\vec{q}, 0)$, at zero frequency which gives us the momentum-frequency space density

$$\mathrm{Re}[\rho(\vec{q}, 0)] = \frac{4\pi \mathrm{e}^2}{q^2}\chi'(\vec{q}, 0). \tag{3.17}$$

Fourier transforming $\rho(\vec{q}, 0)$ from momentum space to real space gives us

$$\rho(x, y, q_z|_0; 0) = \rho_{cloud}(x, y; 0) = \iint_{-\infty}^{\infty} \frac{1}{(2\pi)^2}\rho(\vec{q}, 0)\cos(q_x x + q_y y)\, dq_x dq_y \tag{3.18}$$

the spatially modulating steady-state electron density cloud that dresses a charged impurity (electron, proton, muon, etc.). A fortunate coincidence of our data taking process is that the non-uniform spacing of our measured momentums prevents the Fourier transform from repeating in real space.

We performed numerical integration of $\rho_{cloud}(x, y; 0)$ from zero to incrementally increasing radius as a way to obtain the effective charge screened by the system,

$$Z_{eff} = \int_0^{2\pi}\int_0^R \rho_{cloud}(x, y; 0)\, r\, dr d\theta$$

to a test charge of $Z_{test} = 1$. The integration of the effective charge reaches a plateau at about 17 Å of approximately $Z_{eff} \approx 0.9$. We know from the Friedel sum rule that

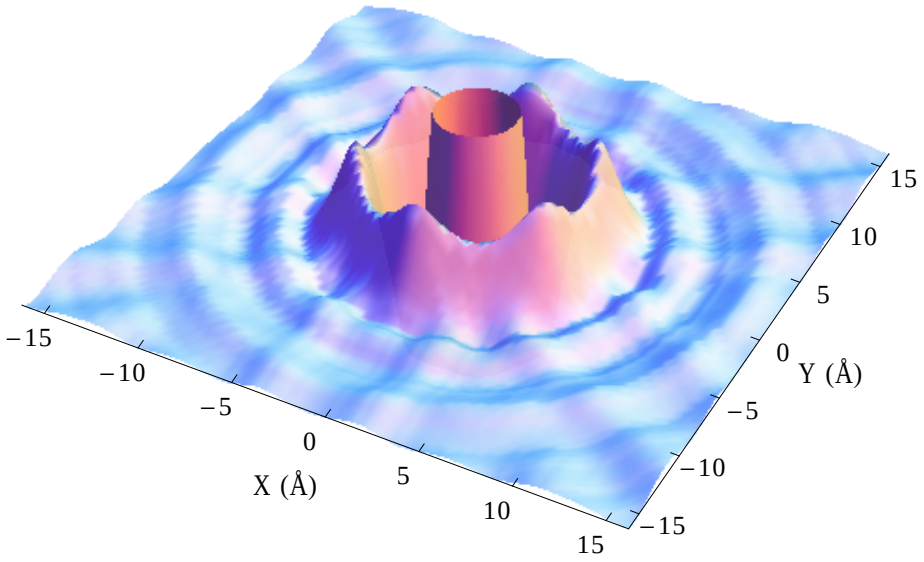

Figure 3.27: Image of the static, steady-state density response of single crystal graphite. Of note is the six-fold symmetry in the local density and that the size of the cloud around the charged impurity is approximately 1 nm.

the charged impurity will be completely screened in metal at some finite radius. In graphite, a semi-metal, the low carrier density predicates that the radius at which the screening becomes unity will be very large, so what we are observing is a separation of length scales. There exists a short length scale in which $\approx 90\%$ of the charge is screened followed by a plateau, which we observe. Beyond the plateau the total charge will begin to rise again until Z_{eff} and Z_{test} are equal. Unfortunately, the range where this unification occurs is well beyond the what we are able to measure experimentally. From the charge density cloud we can calculate the static dielectric screening constant,

$$\epsilon_{\infty} = \frac{Z_{test}}{Z_{test} - Z_{eff}} \tag{3.19}$$

the background upon which the electrons reside. Up to the plateau at 17 Å the

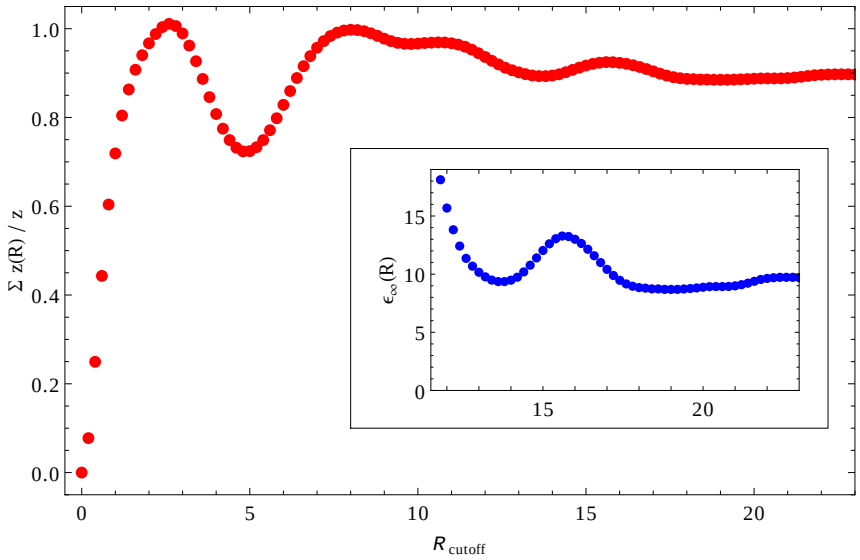

Figure 3.28: Integration of the effective charge seen by the system as a function of the cutoff radius of the integral. The effective charge plateaus around 17 Å to a value of approximately 0.9. The inset shows the calculation of ϵ_∞ as a function of radius. Just as in the charge, ϵ_∞ also plateaus around 17 Å.

dielectric constant is $\epsilon_\infty \approx 9.2$ indicating a very strong screening effect for the semi-metal system. Using this value for ϵ in equation (1.8) would reduce the strength of the correlation strength in graphene by nearly an order of magnitude. While this is only the an estimation for graphene based on graphite, it does offer a qualitative explanation for the problems presented in the introduction as we expect graphene to have a value of ϵ similar to that of graphite.

Examination of the charge density cloud allows us to place a measurement on the size of the quasiparticle structure. The majority of the features present in both the static and dynamical density distributions reside within a 0.7 Å to 0.8 Å radius from center of the quasiparticle which puts the size the spatial extent of the quasiparticle at approximately 1.5 Å.

Dynamics

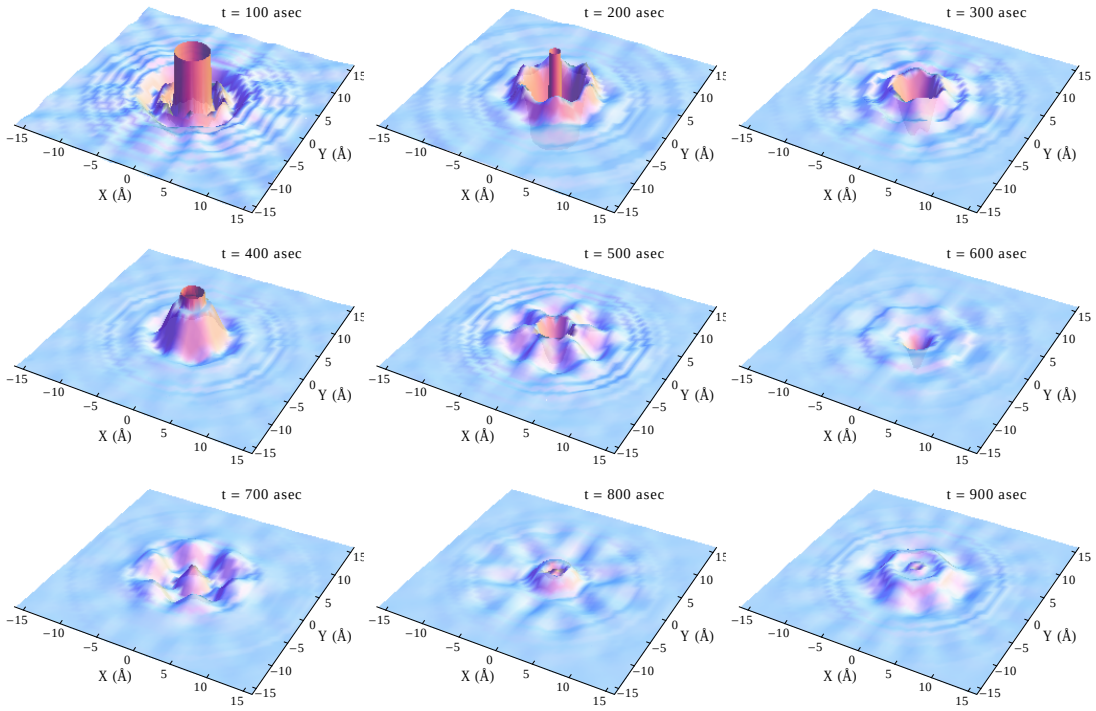

Figure 3.29: The density $\rho_{cloud}(x, y; t)$ at incremental 100 asec time frames from the introduction of the charged impurity at $t = 0$. In essence, this is the birth of a quasiparticle as the local charge density sloshes around in response, trying to dress and screen the charged impurity.

In addition to the static screening, we have also performed extensive calculations to determine the dynamical portion of the electronic screening response, $\rho_{cloud}(x, y; t)$. The method for obtaining $\rho_{cloud}(x, y; t)$ for $t > 0$ is similar to how we calculated $\rho_{cloud}(x, y; t)$ with the major exception of not needing to perform a Kramers-Kronig transformation (see appendix A for details). $\mathrm{Im}[\rho(\vec{q}, \omega)]$ is Fourier transformed from ω to t using

$$\rho(\vec{q}, t) = -\frac{1}{\pi} \int_0^\infty \mathrm{Im}[\rho(\vec{q}, \omega)] \ \sin(\omega\, t/\hbar)\, d\omega \tag{3.20}$$

giving $\rho(\vec{q},t)$ in increments of 10 attoseconds from 10 asec to 1000 asec. We then Fourier transform $\rho(\vec{q},t)$ from $\vec{q}$ to $\{x,y,q_z|_o\}$ using equation (3.18) at each time giving $\rho_{cloud}(x,y,t)$. By weaving together the time slices of the density response we have also created animated visual representations of how the density is responding to a charged impurity as the quasiparticle is born.

The resolution of both the space and time parameters in our inversions are set by the Nyquist theorem [67]. The Nyquist theorem puts a limit on the minimum sampling frequency needed to accurately reconstruct a signal in time that lies within a given bandwidth. We apply this theory backward in that we have measured the signal within a given frequency range and wish to know the smallest step size in time that this can reconstruct. We can express this for both parameters as

$$\delta t \geq \frac{2\pi}{E_r/\hbar} \qquad and \qquad \delta r \geq \frac{2\pi}{q_r} \tag{3.21}$$

where E_r is the energy range and q_r is the momentum range over which we take measurements. We have the fortunate advantage that $\chi''(\vec{q},\omega)$ has symmetry around zero frequency and zero momentum, effectively doubling our energy range, E_r, and momentum range q_r. For the entire experiment we measured energies up to 200 eV, with the doubling factor this corresponds to times steps of $\delta t \geq 10.3$ asec; and we measured momentum up to $q_r = 7.88\,\text{Å}^{-1}$ corresponding to spatial steps of $\delta x \geq 0.399\,\text{Å}$.

We make use of the dynamical density response to gauge how electron medium responds when the charge is moving at constant velocity, akin to the ripples produced when a ball is dragged through water. To image the distortion of the quasiparticle cloud as the charge moves in the plane of a sheet of graphite we convolved the dynamical density function, $\rho_{cloud}(x,y;t)$, with

$$\frac{1}{Z}\delta(\vec{r}-\vec{v}t).$$

at various velocities. Up to at least the Fermi velocity the density cloud that dresses

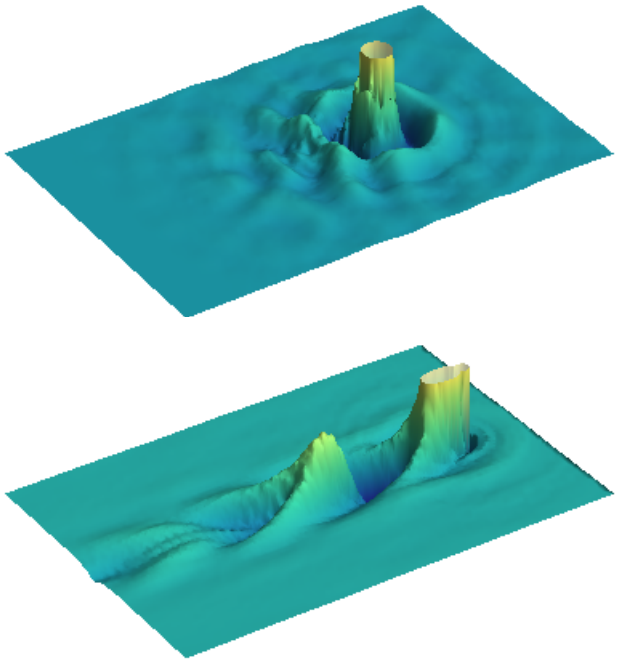

Figure 3.30: **Top:**A charged impurity moving at $v = v_F$. The surrounding density exhibits very little distrubance compared to the stationary case. **Bottom:** The wake produced by a charge moving at $v = 10v_F$. The huge distortion indicates a breakdown of the quasiparticle picture at this speed.

the charged particle remains very rigid, showing very little distortion. However, when the velocity greatly exceeds the Fermi velocity (such as $v = 10v_F$) the quasiparticle cloud begins to break down and a large wake appears behind the charge.

Leading the charge at high velocity is a moderate build up of compressed density modulation. Our analysis investigated the possibility of a critical velocity where the build up of the compressed cloud would become too large and the energy would be released in the equivalent of a sonic boom. However, the quality factor, Q, of the electron medium in graphite is too low to support such a phenomenon (as opposed

to very high Q of air) as we saw no evidence of an "electronic boom" at any velocity.

IV Summary and Discussion

In this body of research we sought to expand Abbamonte's [56] attosecond-resolution electron density imaging technique into multiple dimensions and apply it to the measured energy-loss spectra of graphite as a means of imaging the charge density cloud that surrounds a test charge to form quasiparticles in graphite. Using the expanded computational technique we examined the anisotropic charge structure of a quasiparticle as it is born and evolves in 10 asec time frames. We offer a possible explanation for some of the discrepancies between current experiments and theoretical work on graphene and introduce a conversion technique which enables us to examine the 2-dimensional density-density Green's function from 3-dimensional data.

Summary

We collected data from both a highest grade sample of highly oriented pyrolytic graphite and a unique sample of single crystal graphite using inelastic x-ray scattering. Inelastic x-ray scattering is a powerful technique that measures the energy-loss spectra which is proportional to the density-density Green's function, $\chi''(\vec{q},\omega)$, as a function of two parameters: momentum transfer, $\vec{q}$, and energy or frequency, $E = \hbar\omega$. The highly oriented pyrolytic graphite (HOPG) data is normalized and then scaled using the f-sum rule and the anisotropic part of the single crystal graphite (SCG) data is incorporated into the HOPG data creating a complete data set, $\chi''(\vec{q},\omega)$, for the Basal plane.

We linearly interpolate $\chi''(\vec{q},\omega)$ and use the Kramers-Kronig transformation to get the part, $\chi'(\vec{q},0)$, at zero frequency. We use a 2-dimensional computational Fourier inversion algorithm on $\frac{4\pi e^2}{q^2}\chi'(\vec{q},0)$ to produce $\rho_{cloud}(x,y;0)$, a real-space map of the quasiparticle's charge density cloud at infinite time. Along a parallel vein, we use the

same 2D momentum-real-space inversion algorithm as well as a similar frequency-time Fourier inversion algorithm on $\frac{4\pi e^2}{q^2}\chi''(\vec{q},\omega)$ to produce $\rho_{cloud}(x,y;t)$, a real-space map of the quasiparticle's charge density cloud at 10 asec intervals; combining these time slices creates an animated representation of the quasiparticle's cloud as it forms.

Recent theoretical work on graphene indicates that the band structure at the Dirac points (the K and K' corners of the Brillouin zone) should become very steep and nearly divergent at the crossing points. However, experimental measurements of the many-body density of states (via inverse compressibility probe) and of the band dispersion (via ARPES) have failed to observe this effect. We believe the disparity is the a result of a misconception of the correlation strength, λ, of the electrons. The electron correlation strength is inversely related to the dielectric constant, ϵ, of the system which many theoretical studies have assumed to be between $\epsilon = 1$ and $\epsilon = 1.75$ for graphene. By numerically integrating $\rho_{cloud}(x,y;0)$ to get the effective screened charge, Z_{eff}, we calculated the dielectric constant, $\epsilon_\infty = (Z_{test} - Z_{eff})/Z_{test}$, in graphite to be $\epsilon_\infty \approx 9.2$, nearly an order of magnitude larger than the assumed values. We expect the value of graphene to have a similar size to that of graphite since the inter-layer interaction is predominately governed by a weakened Coulomb interaction and because we measure features at energies much greater than the inter-plane hopping energy; meaning that the energy-loss spectrum of a single layer of graphite, from which ϵ is derived, will be very similar to that of bulk graphite (for in-plane measurements).

Discussion

We have pursued several related goals in our research. Primarily we have demonstrated the applicability of using a multi-dimensional inversion algorithm to image the anisotropy in real-space of the local density response to a charged particle. Ex-

pansion of this technique from 1 dimension to 2-dimensions does increase the amount of computation required by several orders of magnitude; however, this is a relatively small cost. Using graphite as a test system we gathered data using inelastic X-ray scattering to measure electronic features such as plasmons.

Inelastic X-ray scattering is a powerful technique in its own right for measuring the energy loss spectra. Properties of the system, such as the dielectric function, are extracted from the IXS data and give information about how the system's electrons interact in momentum and frequency space. We offer this technique as an additional tool which should be used when real-space and time information of the local charge density is required.

One such application we have also explored is the determination of the background dielectric constant, ϵ_∞, which can be exceedingly difficult to extract via extrapolation to $q = 0$ in momentum space. Here, the second section of our work comes to play. We calculate ϵ_∞ by integrating the real space density obtained from our inversion technique. We integrate the density up to a cutoff radius of $R_c = 25\,\text{Å}$ as this is as far as our momentum resolution permits. However, beyond $R_c = 15\,\text{Å}$ the integral is stable and only fluctuate minutely around the final value. While this sort of numerical approach to calculate ϵ_∞ seems counterintuitive, the extrapolation in momentum space to $q = 0$ is very sensitive to how the extrapolation is performed and to small perturbations in the data. For this reason, we found it was much more robust to error to perform our calculations in real space where the low q data gets pushed out to high radius.

In performing this inversion technique and studying the results, we realized that what we are observing is the charge structure of quasiparticles in graphite. This is the third emphasis of our work; specifically, we have used the inversion to image the in-plane screening process and witness the creation and evolution of a quasiparticle. To

our knowledge this is the first time the internal density structure of a quasiparticle's cloud has been measured and imaged in real-space and time in any dimension. The validity of the quasiparticle underpins many theories of condensed matter physics, so we took this opportunity to test how well the structure of the quasiparticle remains intact. We found that when the quasiparticle is moving at normal velocities (such as up to the Fermi velocity) the structure retains its rigid structure, but when traveling speeds substantially larger than the Fermi velocity the surround cloud distorts and invalidated the quasiparticle concept. This puts a bound on the range of velocities over which the quasiparticle concept is applicable

Future Work

The recent focus on graphene by the world of solid state physics lead us to ask what we can learn about graphene by studying graphite. We want to know, beyond qualitative statements on the nature of screening and quasiparticles in graphene, what an investigation of graphite can tell us about graphene. We wish to make a solid connection between 3-dimensional data taken on graphite and the 2-dimensional graphene system.

There are several key features and an assumptions which allow the possibility to make a comparison between graphite and graphene using our data. First, the electrons in graphite are dominated by the Coulomb interaction between planes, rather than coherent hopping between planes, i.e. the layers are purely van der Waals bonded.. Second, all of the features in our data are at energies much higher than the inter-plane hopping energy, $t_\perp \approx 400$ meV. Third, the in-plane mobility is at least an orders of magnitude greater than the inter-plane mobility in graphite ($mobility_{in\text{-}plane} \gg mobility_{trans\text{-}plane}$). These three features of graphite lead to a description of graphite in which the electrons that are very mobile, but localized in-

plane and interact only very weakly between planes through a long range Coulomb interaction. We make the assumptions that the single particle excitation spectrum are similar for graphite and graphene which is reasonable based on the three properties listed above.

From the standpoint of quantum field theory, what we measure is the *full* susceptibility, χ_{full}, which includes all single-electron excitations and interactions between electrons that are possible. We can diagram χ_{full} as the summation

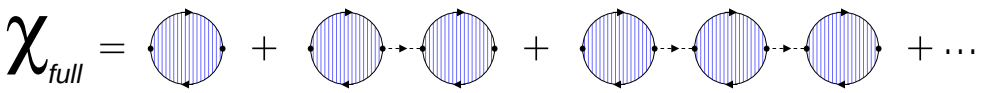

where the filled bubble represents the proper susceptibility, χ^*, diagrammed as the summation over all single-electron excitations

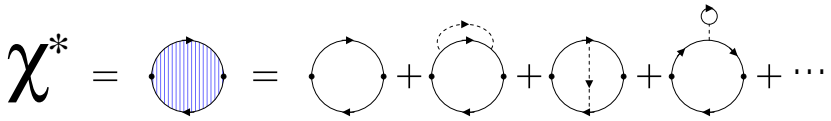

The full susceptibility is the infinite sum of n proper susceptibility bubbles multiplied by its propagator, the Coulomb potential, $V(q)$. This sum reduces to the Dyson equation:

$$\chi_{full}(\vec{q},\omega) = \sum_{n=1}^{\infty} \chi^*(V_d(q)\,\chi^*(\vec{q},\omega))^n = \frac{\chi^*(\vec{q},\omega)}{1 - V_d(q)\,\chi^*(\vec{q},\omega)}. \tag{4.1}$$

where $V_d(q)$ is the Coulomb potential in the d dimensions. Rearranging equation (4.1) to isolate $\chi^*(\vec{q},\omega)$ gives

$$\chi^*(\vec{q},\omega) = \frac{\chi_{full}(\vec{q},\omega)}{1 + V_d(q)\,\chi_{full}(\vec{q},\omega)} \tag{4.2}$$

a simple equation to determine the proper susceptibility from our measurements of the full susceptibility.

If we believe the assumptions made above that the single particle spectra for the two systems look similar, then we should expect that

$$\chi^*_{2D}(\vec{q},\omega) \approx \chi^*_{3D}(\vec{q},\omega). \tag{4.3}$$

To put it another way, if we removed the coulomb interaction, which is how the electrons interact between planes, and only look at the single-electron excitations, then we should predict that the susceptibility of an infinite array of uncoupled graphene sheets will be nearly equal to that of graphite.

Substituting equation (4.2) for both sides of equation (4.3) gives a relation between the full susceptibility of graphite and graphene as

$$\frac{\chi_{2D}(\vec{q},\omega)}{1+V_{2D}(q)\,\chi_{2D}(\vec{q},\omega)} = \chi^*_{2D}(\vec{q},\omega) \approx \chi^*_{3D}(\vec{q},\omega) = \frac{\chi_{3D}(\vec{q},\omega)}{1+V_{3D}(q)\,\chi_{3D}(\vec{q},\omega)}. \tag{4.4}$$

where solving for $\chi_{2D}(\vec{q},\omega)$ yields

$$\chi_{2D}(\vec{q},\omega) = \frac{\chi_{3D}(\vec{q},\omega)}{1+(V_{3D}(q)-V_{2D}(q))(\chi_{3D}(\vec{q},\omega))} \tag{4.5}$$

a method for obtaining the 2-dimensional spectra from the measured 3-dimensional data. The Coulomb potentials in 2D and 3D used in equation (4.5) are given by the generalized Coulomb propagator

$$V(q) = 2\pi d\left(\frac{e^2}{q}\right) S(q_\parallel, q_z) \tag{4.6}$$

$$S(q_\parallel, q_z) = \begin{cases} 1 & \text{[2D]} \\ \frac{\sinh(q_\parallel d)}{\cosh(q_\parallel d)-1} & \text{[3D]} \end{cases}$$

as illustrated by Shung in 1986 [68]. Substituting these three equations for the Coulomb potential into equation (4.5) gives

$$\chi_{2D}(\vec{q},\omega) = \frac{\chi_{3D}(\vec{q},\omega)}{1+\frac{2\pi d\,e^2}{q}\left(\frac{\sinh(q_\parallel d)}{\cosh(q_\parallel d)-1}-1\right)\chi_{3D}(\vec{q},\omega)} \tag{4.7}$$

where $q_{\|}$ is the momentum parallel to the Basal plane and q_z, the out-of-plane momentum, is set to zero.

We apply this formula using a scaling fit parameter, β, to electron energy loss spectroscopy (EELS) data taken by Eberlein, et al. in 2008 [69] on graphite and com-

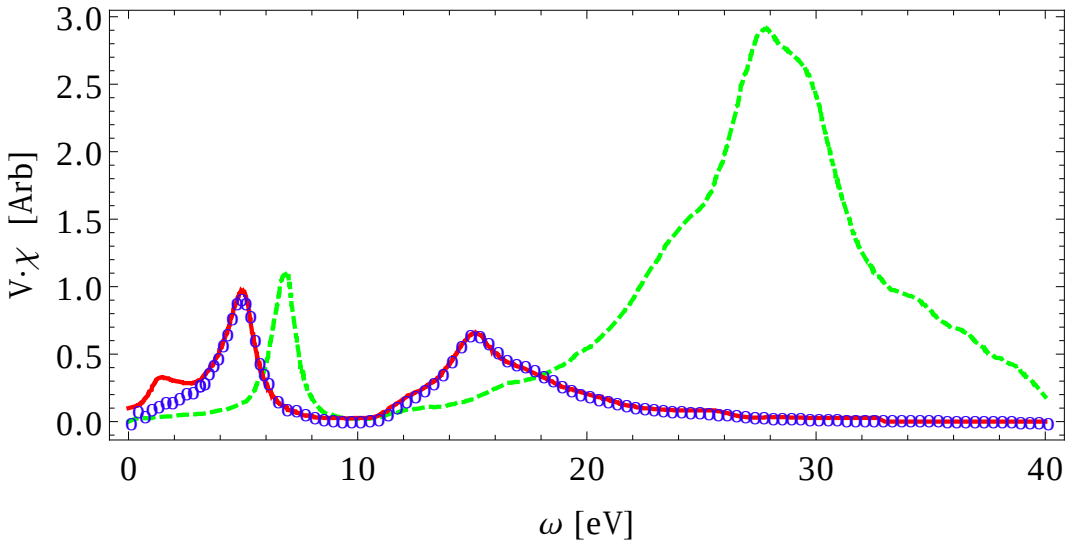

Figure 4.31: Shown above is the EELS data taken by Eberlein, et al. [69] on graphite (dashed green) and a single layer of graphene (solid red). We applied our conversion algorithm to the unscaled graphite data and minimized with respect to the fit parameter, β, to produce the 2D data shown in blue circles. The converted and measured data on graphene are very close to each other.

pare it to their data taken on a single layer of graphene by minimizing the difference between the real and converted data using the fit parameter. Though all of their EELS data we present was taken at the same $\vec{q}$, no explicit value for the momentum vector was given in their study, we therefore used the momentum transfer as a fit variable in the conversion. The match between the converted data and the measured 2D data is very close except at very low energy (we believe the extra bump at low energy in their 2D data comes from an improper removal of the elastic peak), con-

firming our theory and supporting the notion of studying the properties of graphene using graphite.

A future investigation on graphite using converted 3-dimensional graphite data is in progress and would greatly open up the accessibility of graphene studies. This conversion technique is in its infancy, requires a large amount of computation time and the scaling parameter has yet to be fully pinned down, thus preventing us from having already performed the conversion on our anisotropic data. However, the future looks bright for this conversion method and we hope that it will also be able to be applied to other systems with layering similar to that in graphite.

References

[1] L. D. Landau. "The theory of a Fermi liquid." *Soviet Physics JETP*, 3:920–925, 1956.

[2] P. Nozières. *Theory of Interacting Fermi Systems.* W. A. Benjamin, Inc., New York, NY, 1964.

[3] P. Nozières and D. Pines. "Electron Interaction in Solids. General Formulation." *Physical Review*, 109(3), 1958.

[4] P. Nozières and D. Pines. "Electron Interaction in Solids. The Nature of the Elementary Excitations." *Physical Review*, 109(4), 1958.

[5] D. Bohm and D. Pines. "A Collective Description of Electron Interactions: I. Magnetic Interactions." *Phyical Review*, 82(5), 1951.

[6] D. Pines and D. Bohm. "A Collective Description of Electron Interactions: II. Collective vs. Individual Particle Aspects of the Interactions." *Phyical Review*, 85(2), 1951.

[7] D. Bohm and D. Pines. "A Collective Description of Electron Interactions: III. Coulomb Interactions in a Degenerate Electron Gas." *Phyical Review*, 92(3), 1953.

[8] D. Emin. "Optical properties of large and small polarons and bipolarons." *Phys. Rev. B*, 48(18), 1993.

[9] P. W. Anderson. "Hall Effect in the Two-Dimensional Luttinger Liquid." *Phys. Rev. Letters*, 67(15), 1991.

[10] J. L. Levy and R. B. Laughlin. "Spin susceptibility and gap structure of the fractional-statistics gas." *Phys. Rev. B*, 50(10), 1994.

[11] F. Mohling and I. Rama Rao. "Degenerate Bose System. IV. Quasiparticle Model." *Physical Review*, 136(4A), 1964.

[12] A. B. Migdal. *Nuclear Theory: The Quasiparticle Method.* W. A. Benjamin, New York, NY, 1968.

[13] G. Giuliani and G. Vignale. *Quantum Theory of the Electron Liquid.* Cambridge University Press, 2005.

[14] D. Pines. *Elementary Excitations in Solids.* W. A. Benjamin, Inc., New York, NY, 1963.

[15] B. Batlogg, H. Y. Hwang, H. Takagi, R. J. Cava, H. L. Kao, and J. Kwo. "Normal State Phase Diagram of $(La,Sr)_2Cu0_4$ from Charge and Spin Dynamics." *Physica C*, 235-240:130–133, 1994.

[16] Z. Fisk, J. L. Sarrao, J. L. Smith, and J. D. Thompson. "The physics and chemistry of heavy fermions." *Proc. Natl. Acad. Sci. USA*, 92:6663–6667, July 1995.

[17] S. Sinnott and R. Andrews. "Carbon Nanotubes: Synthesis, Properties, and Applications." *Critical Reviews in Solid State and Materials Sciences*, 26(3):145–249, 2001.

[18] B. G. Demczyk, Y. M. Wang, J. Cumings, M. Hetman, W. Han, A. Zettl, and R. O. Ritchie. "Direct mechanical measurement of the tensile strength and elastic modulus of multiwalled carbon nanotubes." *Mat. Sci. and Eng. A*, 334:173–178, 2002.

[19] V. N. Nikitin, S. I. Kiselev, T. N. Popova, V. M. Maslyuk, and V. Kolesnikov. "New Weldable High-Strength Wear-Resistant Steel with a Minimum Tensile Strength of 1050 N/mm^2." *Metallurgist*, 49, 2005.

[20] H. D Wagner. *Encyclopedia of Polymer Science and Technology - Reinforcement*, volume 4. Wiley-Interscience, 2003.

[21] N. Ashcroft and N. Mermin. *Solid State Physics*. Harcourt Canada, Limited, 1976.

[22] A. Geim and A. MacDonald. "Graphene: Exploring carbon flatland." *Physics Today*, pages 35–41, August 2007.

[23] P. R. Wallace. "The Band Theory of Graphite." *Physical Review*, 71(9), 1947.

[24] A. H. Compton. "The Spectrum of Scattered X-Rays." *Physical Review*, 22(5):409–413, 1923.

[25] J. C. Slonczewski and P. R. Weiss. "Band Structure of Graphite." *Physical Review*, 109(2), 1958.

[26] J. W. McClure. "Band Structure of Graphite and de Haas-van Alphen Effect." *Physical Review*, 108(3), 1957.

[27] T. Ohta, A. Bostwick, J. L. McChesney, T. Seyller, K. Horn, and E. Rotenberg. "Interlayer Interaction and Electronic Screening in Multilayer Graphene Investigated with Angle-Resolved Photoemission Spectroscopy." *Phys. Rev. Letters*, 98(206802), 2007.

[28] K. S. Novoselov, D. Jiang, F. Schedin, T. J. Booth, V. V. Khotkevich, S. V. Morozov, and A. K. Geim. "Two-dimensional atomic crystals." *Proc. Nat. Acad. Sci. USA*, 102(30), July 2005.

[29] A. H. Castro Neto, F. Guinea, N. M. R. Peres, K. S. Novoselov, and A. K. Geim. "The electronic properties of graphene." *arXiv [cond-mat.other]*, 0709.1163v2, 2008.

[30] K. S. Novoselov, A. K. Geim, D. Jiang, Y. Zhang, S. V. Dubonos, I. V. Grigorieva, and A. A. Firsov. "Electric Field Effect in Atomically Thin Carbon Films." *Science*, 306, October 2004.

[31] E. Fradkin. "Critical behavior of disordered degenerate semiconductors. II. Spectrum and transport properties in mean-field theory." *Phys. Rev. B*, 33(5):3263, 1986.

[32] M. Lemme, M. Echtermeyer, M. Baus, and H. Kurz. "A Graphene Field-Effect Device." *IEEE Elec. Dev. Letters*, 28(4), 2007.

[33] G. Liu, W. Stillman, S. Rumyantsev, Q. Shao, M. Shur, and A. A. Ballandin. "Low-frequency electronic noise in the double-gate single-layer graphene transistors." *Appl. Phys. Lett.*, 95(033103), 2009.

[34] Q. Zhang, T. Fang, H. Xing, A. Seabaugh, and D. Jena. "Graphene Nanoribbon Tunnel Transistors." *IEEE Elec. Dev. Letters*, 29(12), 2008.

[35] R. Miranda and L. Vázquez de Parga. "Surfing ripples towards new devices." *Nature Nanotech.*, 4:549–550, 2009.

[36] F. Guinea, M. I. Katsnelson, and A. K. Geim. "Energy gaps and a zero-field quantum Hall effect in graphene by strain engineering." *Nature Physics*, DOI: 10.1038/NNANO.2009.292, 2009.

[37] F. Xia, T. Mueller, Y. Lin, A. Valdes-Garcia, and P. Avouris. "Ultrafast graphene photodector." *Nature Nanotech.*, DOI: 10.1038/NNANO.2009.292, 2009.

[38] P. Gava, M. Lazzeri, A. Saitta, and F. Mauri. "Ab initio study of gap opening and screening effects in gated bilayer graphene." *Phys. Rev. B*, 79(165431), 2009.

[39] L. A. Falkovsky. "Screening in gated bilayer graphene." *Phys. Rev. B*, 80(113413), 2009.

[40] X. Wang and T. Chakraborty. "Coulomb screening and collective excitations in a graphene bilayer." *Phys. Rev. B*, 75(041404), 2007.

[41] E. H. Hwang and S. Das Sarma. "Dielectric function, screening, and plasmons in two-dimensional graphene." *Phys. Rev. B*, 75(205418), 2007.

[42] V. Pereira, J. Nilsson, and A. H. Castro Neto. "Coulomb Impurity Problem in Graphene." *Phys. Rev. Letters*, 99(166802), 2007.

[43] V. N. Kotov, B. Uchoa, and A. H. Castro Neto. "Electron-electron interactions in the vacuum polarization of graphene." *Phys. Rev. B*, 78(035119), 2008.

[44] V. M. Pereira, V. N. Kotov, and A. H. Castro Neto. "Supercritical Coulomb impurities in gapped graphene." *Phys. Rev. B*, 78(085101), 2008.

[45] M. Polini, A. Tomadin, R. Asgari, and A. H. MacDonald. "Density functional theory of graphene sheets." *Phys. Rev. B*, 78(115426), 2008.

[46] J. González, F. Guinea, and M. A. H. Vozmediano. "Non-Fermi liquid behavior of electrons in the half-filled honeycomb lattice (A renormalization group approach)." *Nucl. Phys. B*, 424:595–618, 1994.

[47] E. H. Hwang, Ben Yu-Kuang Hu, and S. Das Sarma. "Density Dependent Exchange Contribution to $\partial\mu/\partial n$ and Compressibility in Graphene." *Phys. Rev. Letters*, 99(226801), 2007.

[48] A. Grüneis, C. Attaccalite, T. Pichler, V. Zabolotnyy, H. Shiozawa, S. L. Molodtsov, D. Inosov, A. Koitzsch, M. Knupfer, J. Schiessling, R. Follath, R. Weber, P. Rudolf, L. Wirtz, and A. Rubio. "Electron-Electron Correlation in Graphite: A Combined Angle-Resolved Photoemission and First-Principles Study." *Phys. Rev. Letters*, 100(037601), 2008.

[49] S. Y. Zhou, G. Gweon, J. Graf, A. V. Federov, C. D. Spararu, R. D. Diehl, Y. Kopelevich, D. Lee, S. G. Louie, and A. Lanzara. "First direct observation of Dirac fermions in graphite." *Nature Physics*, 2, September 2006.

[50] A. Bostwick, T. Ohta, T. Seyller, K. Horn, and E. Rotenberg. "Quasiparticle dynamics in graphene." *Nature Physics*, 3, January 2007.

[51] A. Grüneis, C. Attaccalite, L. Wirtz, H. Shiozawa, R. Saito, T. Pichler, and A. Rubio. "Tight-binding description of the quasiparticle dispersion of graphite and few-layer graphene." *Phys. Rev. B*, 78(205425), 2008.

[52] J. Martin, N. Akerman, G. Ulbricht, T. Lohmann, J. H. Smet, K. Von Klitzing, and A. Yacoby. "Observation of electron-hole puddles in graphene using a scanning single-electron transistor." *Nature Physics*, 4, February 2008.

[53] Y. Barlas, T. Pereg-Barnea, M. Polini, R. Asgari, and A. H. MacDonald. "Chirality and Correlations in Graphene." *Phys. Rev. Letters*, 98(236601), 2007.

[54] D. Sheehy and J. Schmalian. "Quantum Critical Scaling in Graphene." *Phys. Rev. Letters*, 99(226803), 2007.

[55] R. Asgari, M. M. Vazifeh, M. R. Ramezanali, E. Davoudi, and B. Tanatar. "Effect of disorder on the ground-state properties of graphene." *Phys. Rev. B*, 77(125432), 2008.

[56] P. Abbamonte, K. D. Finkelstein, M. D. Collins, and S. M. Gruner. "Imaging Density Disturbances inWater with a 41.3-Attosecond Time Resolution." *Phys. Rev. Letters*, 92(237401), 2004.

[57] P. M. Platzman and P. Eisenberger. "Presence of an Incipient Wigner Electron Lattice in Solid-State Electron Gases." *Phys. Rev. Letters*, 33(3), 1974.

[58] P. Eisenberger and P. M. Platzman. "Larbe anisotropy in the dynamic structure factor of graphite." *Phys. Rev. B*, 13(2), 1976.

[59] R. A. Bonham. "Calculation of total inelastic x-ray scatter cross sections $(d\sigma/d\Omega)_{inel}$." *Phys. Rev. A*, 23(6), 1981.

[60] W. Schülke, H. Nagasawa, and S. Mourikis. "Dynamic Structure Factor of Electrons in Li by Inelastic Synchrotron X-Ray Scattering." *Phys. Rev. Letters*, 51(23), 1984.

[61] W. Schülke, H. Nagasawa, S. Mourikis, and P. Lanzki. "Dynamic structure of electrons in Li metal: Inelastic synchrotron x-ray scattering results and interpretation beyond the random-phase approximation." *Phys. Rev. B*, 33(10), 1986.

[62] W. Schülke, U. Bonse, H. Nagasawa, A. Kaprolat, and A. Berthold. "Interband transitions and core excitation in highly oriented pyrolytic graphite studied by inelastic synchrotron x-ray scattering: Band-structure information." *Phys. Rev. B*, 38(3), 1988.

[63] Momentive Performance Materials, www.momentive.com. *Graphite Monochromators.*

[64] N. Hiraoka, H. Ishii, I. Jarrige, and Y. Q. Cai. "Inelastic x-ray scattering studies of low-energy charge excitations in graphite." *Phys. Rev. B*, 72(075103), 2005.

[65] S. Rabii, J. Chomilier, and G. Loupias. "Polarization of carbon electron-momentum density in lithium-graphite intercalation compounds." *Phys. Rev. B*, 40(15), 1989.

[66] H. Reniewicz, A. Andrejczuk, M. Brancewicz, E. Żukowski, L. Dobrzyński, and S. Kaprzyk. "Electron momentum density of hexagonal cadmium studied by Compton scattering." *Phys. Stat. Sol. B*, 241(8), 2004.

[67] P. Abbamonte, T. Graber, J. P. Reed, S. Smadici, C.-L. Yeh, A. Shunkla, J.-P. Rueff, and Wei Ku. "Dynamical reconstruction of the exciton in LiF with inelastic x-ray scattering." *Proc. Nat. Acad. Sci. USA*, 105(34), 2008.

[68] K. W. Shung. "Lifetime effects in low-stage intercalated graphite systems." *Phys. Rev. B*, 34(2), 1986.

[69] T. Eberlein, U. Bangert, R. R. Nair, R. Jones, M. Gass, A. L. Bleloch, K. S. Novoselov, A. Geim, and P. R. Briddon. "Plasmon spectroscopy of free-standing graphene films." *Phys. Rev. Bb*, 77(233406), 2008.

Appendix A: Frequency-Time Fourier Transform

The relation between the real part, imaginary part, and full density-density Green's function in time is explained here. We make use of the resulting simplified form of the frequency-time Fourier transform, which lets us skip performing a full computation of the real part of $\chi(\vec{q},\omega)$, in our analysis.

The Kramers-Kronig equation relates the relates the real part of $\chi(\vec{q},\omega)$ to the imaginary part via:

$$\chi'(\vec{q},\omega) = \frac{1}{\pi}\,\mathcal{P}\int_{-\infty}^{\infty} d\omega'\,\frac{\omega'\,\chi''(\vec{q},\omega')}{\omega'^{\,2}-\omega^2} \tag{A.1}$$

given that $\chi(\vec{q},\omega)$ is hermitian in ω. We can write $\chi(\vec{q},t)$ as a Fourier transform of $\chi(\vec{q},\omega)$ to get:

$$\chi(\vec{q},t) = \frac{1}{2\pi}\int_{-\infty}^{\infty} d\omega\,\mathrm{e}^{i\omega t}\chi(\vec{q},\omega) \tag{A.2}$$

which when expanded using the Euler equation gives:

$$\chi(\vec{q},t) = \frac{1}{2\pi}\int_{-\infty}^{\infty} d\omega\,\big(\chi'(\vec{q},\omega)\cos(\omega t) - \chi''(\vec{q},\omega)\sin(\omega t)\big) + 0 \tag{A.3}$$

where the other terms in the integrand go to zero since the imaginary part of the integral is odd. Substituting in $\chi'(\vec{q},\omega)$ from the Kramers-Kronig relation into the first half of the integral gives:

$$\chi(\vec{q},t) = \frac{1}{2\pi}\int_{-\infty}^{\infty} d\omega\,\left[\left(\frac{1}{\pi}\mathcal{P}\int_{-\infty}^{\infty} d\omega'\frac{\omega'\,\chi''\,(\vec{q},\omega')}{\omega'^{\,2}-\omega^2}\right)\cos(\omega t) - \chi''(\vec{q},\omega)\sin(\omega t)\right]. \tag{A.4}$$

This pulls the explicit dependence of the integral out of the Green's function. It also removes the real part of $\chi(\vec{q},\omega)$ from the equation, meaning we can just use the imaginary part which is what we measure. We are now able to change the order of

integration of the first term in the integral over ω such that we may write

$$\chi(\vec{q},t) = \frac{1}{2\pi}\frac{1}{\pi}\,\mathcal{P}\int_{-\infty}^{\infty} d\omega'\,\omega'\,\chi''(\vec{q},\omega')\left(\int_{-\infty}^{\infty} d\omega\,\frac{1}{\omega'^{\,2}-\omega^2}\cos(\omega t)\right) \\ -\frac{1}{2\pi}\int_{\infty}^{\infty} d\omega\,\chi''(\vec{q},\omega)\sin(\omega t) \tag{A.5}$$

The internal integral is of a known form,

$$\int_{-\infty}^{\infty} d\omega\,\frac{1}{\omega'^{\,2}-\omega^2}\cos(\omega t) = \frac{\pi}{i\,\omega'}\mathrm{e}^{-i\,\omega' t} \tag{A.6}$$

which, upon expanding the exponential, gives:

$$\chi(\vec{q},t) = \frac{1}{2\pi}\frac{1}{\pi}\,\mathcal{P}\int_{-\infty}^{\infty} d\omega'\,\omega'\,\chi''(\vec{q},\omega')\left(\frac{\pi}{i\,\omega'}\Big(\cos(\omega' t) - i\sin(\omega' t)\Big)\right) \\ -\frac{1}{2\pi}\int_{\infty}^{\infty} d\omega\,\chi''(\vec{q},\omega)\sin(\omega t) \tag{A.7}$$

We cancel the π, i, and ω' and recall that $\chi''(\vec{q},\omega)$ is an odd function and will integrate to zero when multiplied by the cosine term. This gives us

$$\chi(\vec{q},t) = -\frac{1}{2\pi}\,\mathcal{P}\int_{-\infty}^{\infty} d\omega'\,\chi''(\vec{q},\omega')\sin(\omega' t) - \frac{1}{2\pi}\int_{\infty}^{\infty} d\omega\,\chi''(\vec{q},\omega)\sin(\omega t). \tag{A.8}$$

We use a simple variable substitution of ω for ω' in the first integral and realize that there are no poles or discontinuities in the integrand of the first integral. This leaves the principal value equal to the integral by the definition of the principal value

$$\mathcal{P}\int_a^b dx f(x) \equiv \lim_{\epsilon\to 0^+}\left[\int_a^{c-\epsilon} dx\,f(x) + \int_{c+\epsilon}^{b} dx\,f(x)\right] \qquad a \le c \le b. \tag{A.9}$$

Combining this we arrive at our final equation for the full time-dependent $\chi(\vec{q},t)$ as an integral over just our measured data, $\chi''(\vec{q},\omega)$:

$$\chi(\vec{q},t) = -\frac{1}{\pi}\int_{-\infty}^{\infty} d\omega\,\chi''(\vec{q},\omega)\,\sin(\omega t) \tag{A.10}$$

Appendix B: Momentum Resolution

To determine the momentum resolution of an inelastic X-ray scattering experiment we analyze the geometry of the incoming and scattered X-rays, the analyzer, and the position of the *tth* arm. In the lab frame the initial X-rays have momentum of magnitude $k_0 = E_i/\hbar c = 4.548\,\text{Å}$ (where $E_i = 8.9805$ keV is the incident beam energy) along the direction

$$\vec{k}_i^{(L)} = k_0 \hat{z}^{(L)}$$

and scatters from the sample to an angle *tth* such that the scattered X-rays have momentum

$$\vec{k}_s^{(L)} = k_0(\sin tth\, \hat{x}^{(L)} + \cos tth\, \hat{z}^{(L)})$$

where $\hat{x}$, $\hat{x}$ and $\hat{x}$ are the unit vectors in momentum space. This gives the momentum transferred to the sample in the lab frame as

$$\vec{q}^{(L)} = \vec{k}_i^{(L)} - \vec{k}_s^{(L)} = 2k_0 \sin\frac{tth}{2}\left(\cos\frac{tth}{2}\,\hat{x}^{(L)} - \sin\frac{tth}{2}\,\hat{z}^{(L)}\right). \tag{B.1}$$

Here we will define the sample frame such that $\hat{z}^{(s)}$ always point parallel to the

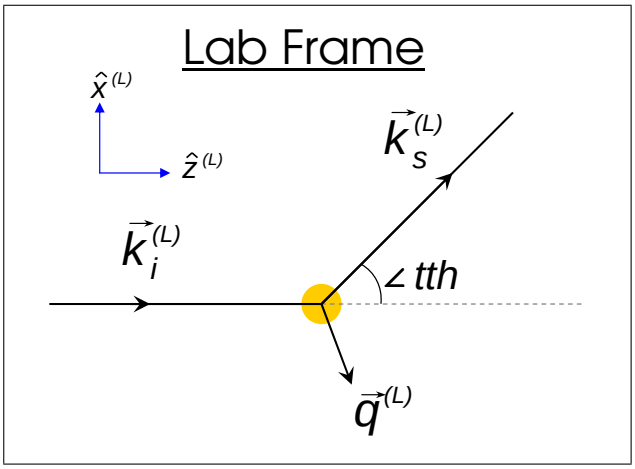

Figure B.32: The lab frame of a scattering experiment with the incident, scattered and transferred momentum vectors labelled.

momentum transfer vector $\vec{q}$ where

$$\vec{q}^{(s)} = 2k_0 \sin\frac{tth}{2}\,\hat{z}^{(s)}. \tag{B.2}$$

The axes are rotated by -$(\pi + tth/2)$ to maintain this orientation for all values of tth.

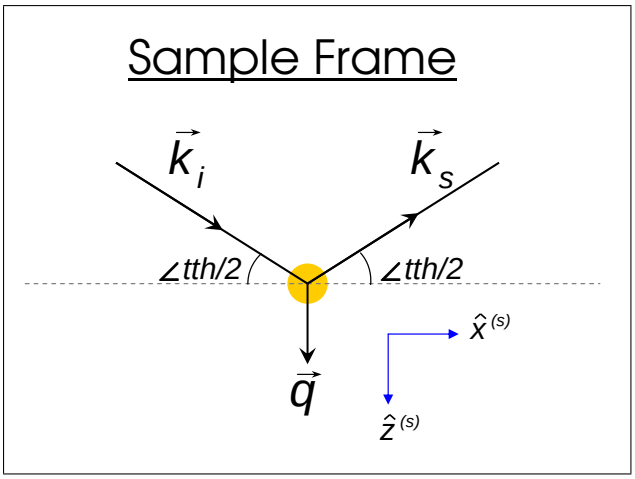

Figure B.33: The sample frame of a scattering experiment with $\vec{q}$ axis lying along $\hat{z}^{(s)}$.

At this point we will drop the use of the (s) superscript and simply use the non-notated coordinates as the sample coordinates. Thus far we have the base dependence of how $\vec{q}$ varies with the angle of the two-theta arm tth. What mainly broadens our resolution is the size of the analyzer which reflects the X-rays. The analyzer introduces a spread in angle $\delta\theta$ which must be accounted for in our equations. What happens physically is that X-rays with a slight higher and lower momentum transfer will reflect off the top and bottom of the analyzer respectively. The higher momentum vector, $\vec{q}_+$, is slightly longer than $\vec{q}$ and is angled to have a small component in the $+\hat{x}$ direction; the reverse is true for the lower momentum vector, $\vec{q}_-$, as shown below in Figure B.34. We can write the transferred momentums $\vec{q}_+$ and $\vec{q}_-$ in the sample

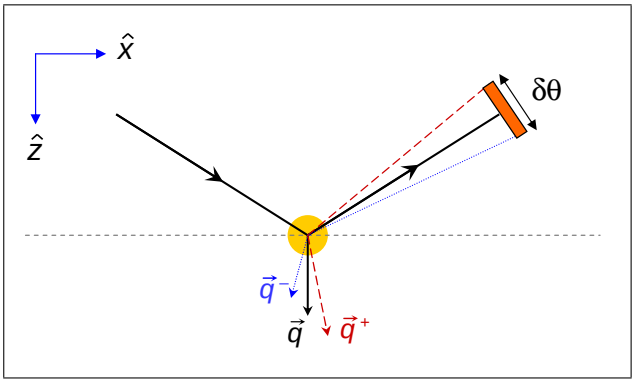

Figure B.34: The angular spread of the analyzer, $\delta\theta$, causes a spread in the transferred momentum, $\vec{q}$. Reflections from the lowest part of the analyzer have a slightly shorter momentum vector (shown in dotted blue as $\vec{q}_{-}$), where reflections from the upper portion of the analyzer have a slightly longer momentum vector (shown in dashed red as $\vec{q}_{+}$)

frame as the set of equations:

$$\vec{q}_{+} = 2k_0 \sin\frac{tth + \delta\theta/2}{2}\Big(\sin(\delta\theta/2)\ \hat{x} + \cos(\delta\theta/2)\ \hat{z}\Big) \tag{B.3}$$

$$\vec{q}_{-} = 2k_0 \sin\frac{tth - \delta\theta/2}{2}\Big(-\sin(\delta\theta/2)\ \hat{x} + \cos(\delta\theta/2)\ \hat{z}\Big). \tag{B.4}$$

While we have restricted this to only two directions for simplicity ($\hat{x}$ and $\hat{z}$), the $\hat{y}$ direction can easily be substituted for the $\hat{x}$ direction since the analyzer is circular.

For any given angle of tth, equations (B.3) and (B.4) plotted on a momentum space map (k_x,k_z) form a line segment. By rotating this line segment about a perpendicular axis through its center, we sweep out a flat disk that represents the momentum resolution of a perfectly collimated, monochromatic source in (k_x,k_y,k_z). However, our experiment is not monochromatic, but has a finite bandwidth set by the energy resolution. This acts to slightly broaden k_0 by

$$\delta k = k_0 \frac{\Delta E}{E} = 1.51 \times 10^{-4}\ \text{Å}. \tag{B.5}$$

This broadening adds a slight thickness to the momentum resolution changing it from a disk to a pancake. The projection of the momentum resolution pancake onto the

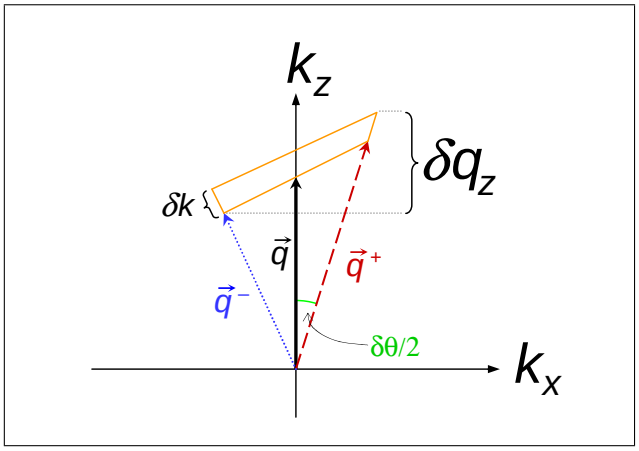

Figure B.35: The momentum vectors $\vec{q}$, $\vec{q}_-$, and $\vec{q}_+$ are plotted in momentum space. The bandwidth broadening, δk, is then added along the directions of each q vector, creating the 4 corners of the quadrilateral (drawn in light orange) that defines the momentum resolution. Rotating the quadrilateral sweeps out a thin "pancake" of momentum resolution.

k_z axis defines the resolution for that momentum direction, δq_z, at a particular angle of tth.